High Energy Pulse Amplification in Mid-IR Range Using Er:ZBLAN Fibers

by

Weizhi Du

A dissertation submitted in partial fulfillment
of the requirements for the degree of
Doctor of Philosophy
(Electrical and Computer Engineering)
in the University of Michigan
2022

Doctoral Committee:

        Professor Almantas Galvanauskas, Chair
        Professor Igor Jovanovic
        Research Scientist John A. Nees
        Professor Herbert G. Winful

Weizhi Du

wzd@umich.edu

ORCID iD: 0000-0001-7448-8190

Dedicated to my family and friends

ACKNOWLEDGEMENTS

I would like to thank all the people who have guided, supported, and accompanied me during my academic journey at the University of Michigan. If someone is missed in this list, he or she must be hided in my heart.

First, I would like to appreciate Professor Galvanauskas who is the most important person during my PhD study. I have been fortunate to be working with such a knowledgeable, enthusiastic, and supportive research adviser. Whenever my research progress was stuck, he always provided a great guidance to help me go across the barrier with patience. He is also a successful model showing me how to balance the career and family. The invaluable skills I have learned from you will be carried with me in the whole life.

I would like to thank my dissertation committee members. Thank you, Professor Jovanovic for your collaboration with our group and providing KTA-based OPO/OPA setup for our initial experiment. Thank you John Nees for constantly bringing in your unique perspectives and helping and advising me with your creative ideas. Thank you Professor Winful for all the brilliant derivations in your lectures EECS 538 and EECS 634. These essential knowledges of

Table of Contents

LIST OF TABLES

LIST OF FIGURES

ABSTRACT

Laser sources operating in Mid-IR (2 – 5 µm) spectral range have many important applications in spectroscopy (e.g. environmental monitoring), medicine (e.g. laser surgery), and fundamental science (e.g. attosecond pulse generation and metrology). Fiber lasers offer technological advantages of high efficiency, compactness, stability, and high mode quality, but typically operate in Near-IR spectral range, because they are based on technologically-mature fused-silica glass which is ill-suited for signal transmission beyond 2µm.

This thesis explores high energy pulse generation in Mid-IR (~3µm) using ZBLAN glass based optical fiber lasers. ZBLAN glasses are becoming the material of choice for fiber lasers accessing mid-IR, since their transmission-window long-wavelength edge extends to ~4 µm, much longer than that of fused-silica glass. Our work focused on Er-doped ZBLAN fibers, which offer significant practical advantages, such as compatibility with standard telecom-grade pump diodes operating at 980nm, where pump-to-signal conversion efficiency can exceed quantum defect limit due to beneficial energy transfer up-conversion processes, and thus leads to record high average powers in Mid-IR.

The main achievement of this work is that we extended ns-scale pulsed energies achievable with Er:ZBLAN fiber by an order of magnitude (from ~10^2 µJ to ~1mJ) while preserving diffraction-limited (i.e. single transverse mode) output beam quality. This was enabled by using Er:ZBLAN fibers with core sizes of 30µm and 50µm which significantly exceed single-mode limit, and

developing techniques of preserving single-mode propagation of high energy pulses in these large mode area fibers. This work serves as the basis for the ongoing work on developing the first femtosecond-pulse fiber CPA system operating in Mid-IR spectral region, as well as for future work on spatial and temporal coherent combining of multiple Mid-IR fiber lasers.

As a related effort, we proposed and simulated several novel machine learning algorithms to optimize coherent pulse stacking (CPS) performance. CPS is a coherent time domain pulse combining technique. Among all methods, we find that the MSPGD achieves best performance and can be potentially advantageous for CPS to increase the system operation efficiency.

Chapter 1 Introduction

1.1 Background and motivation

Albert Einstein first described stimulated emission processes in his 1916 paper [1], which became the foundation for the new type of light sources (quantum light generators - masers and lasers) only in 1950s. In 1951, Charles H. Townes [2] suggested that stimulated emission at microwave frequencies could oscillate in a resonant cavity, and thus can be used to produce coherent electromagnetic radiation. In 1954, Townes and his student James Gordon [3] directed excited ammonia molecules into a resonant cavity to demonstrate the first microwave maser, which oscillated at 24 GHz. Theodore Maiman developed the first red laser emission from a ruby crystal (chromium-doped corundum) in 1960 [4]. Following this breakthrough hundreds of crystals and glasses doped with rare-earth ions have been used for generating coherent laser emission at different wavelengths. Over the past half century laser technology has made tremendous progress, and at present lasers are found almost everywhere in daily life. Lasers had become an integral part of modern society, being used for many applications in manufacturing, construction, telecommunication, automotive technology, medicine, security, etc. Depending on the type of gain medium, lasers can be classified into several different types - gas lasers, solid-state lasers, fiber lasers, liquid (dye) lasers, and semiconductor lasers (laser diodes). Fiber lasers are known as being robust, compact, efficient, high power, and producing high quality

(diffraction-limited) beams, and are thus widely used in various high power and high energy laser systems.

Over the past two decades, there was a continuous increase in fiber laser power. In the late 1990s, the output power of fiber lasers was on the order of 10W, while by the 2010s powers of up to 100kW have been achieved [5]. This was achieved using ytterbium-doped silica-glass fiber (YDF) lasers. The light emission at ~1µm of YDF lasers is via an electronic transition ($^2F_{7/2}$ $\rightarrow$ $^2F_{5/2}$), which provides with a small quantum defect, thus minimizing heat generation, and also has a negligible excited state absorption and non-radiative decay [4]. Other rare-earth-doped fused-silica glass fiber lasers also have been demonstrated to produce relatively high powers [5,6]. However, fused silica fiber has transmission cutoff at around 2µm [8], and thus cannot be used for lasers and amplifiers operating in mid-IR.

In contrast to silica glass, fluoride and chalcogenide glasses have low phonon energy, and thus are transparent in mid-infrared spectral range. Rare-earth doping of these host glasses can provide with multiple lasing transitions in mid-IR. Among these, Er:ZBLAN fiber lasers operating at around 3 µm have a number of advantageous properties, and thus had attracted a considerable of research.

1.2 Applications of Mid-IR and LWIR laser sources

The spectral regions of Mid-IR and LWIR have many different applications. This section summarizes some of the most promising applications for Mid-IR and LWIR laser sources.

Medicine

Lasers operating around 3 µm have great potential for medical applications as a replacement of traditional surgical tools, since they have capability of cutting at the level of a single cell [9]. This is because the fundamental stretching vibration of OH bond is located at ~3 µm, and water is the dominant constituent in soft tissue. Fig. 1.1 shows the water absorption spectrum, indicating that the absorption coefficient reaches ~10000 cm^{-1} at ~2.8 µm, constituting the highest absorption peak in infrared. Therefore, laser radiation at ~3 µm can be effectively absorbed by soft tissue, which enables the minimum wound size [10]. For example, the width of the scars formed from the wounds made by an ultrafast mid-IR laser were half the size of the scars produced using scalpel [9].
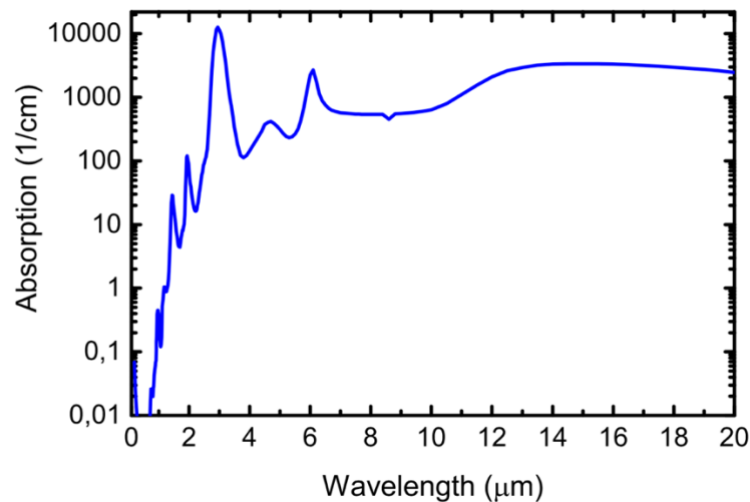
Figure 1. 1: Absorption spectrum of liquid water. [10]

CO$_2$ laser is still most popular for medical applications. However, bulk Er:YAG systems operating at 2.94 µm have started to replace CO$_2$ lasers, since water absorbs ten times more at

2.94 µm than at 10 µm, as shown in Fig. 1.1. Er:YAG laser systems have already been successfully applied into several medical areas such as dermatology, otolaryngology, dentistry, ophthalmology, biopsy, lithotripsy, angioplasty and osteotomy [11-18]. In general, different cell tissue requires different laser power and energy. Hard tissues, such as bone and dental enamel, need high power CW and pulsed 3 µm lasers. For soft tissues lower power lasers can be used, since the mechanisms of laser-tissue interactions there are different from those in the hard tissues, and involve photo-disruption, plasma-induced ablation, thermal, photochemical, and photoablation [19]. Apart from the optical power, it is also essential to control laser exposure time for achieving high process quality. For instance, photochemical, thermal effects need continuous wave (CW) or microsecond pulse duration lasers, while plasma-induced ablation and photo-disruption needs the nanosecond range pulse duration. Moreover, there are some other medical applications requiring shorter pulses at ~3µm, such as optical or corneal transplant surgery, and stapes surgery. In 2007, it was shown that 3 µm ultrafast lasers have a great potential for damage-free medical applications [9].

Fiber laser operating at 3 µm have a great potential to replace the Er:YAG in some specific areas, because they have several advantages for medical applications. In 2000 a CW Er^{3+} doped fiber laser operating at ~3µm was demonstrated to ablate chicken breast tissues [20]. Incisions have been rapidly made without carbonization or charring. Moreover, rare-earth doped fluoride fiber lasers could be tuned to achieve laser emission at specific wavelengths around 3 µm to provide precise control of the beam penetration depth.

Spectroscopy

The MIR spectral range, in particular the range from 2.5 µm to 5µm, is the well-known molecular fingerprint region, within which majority of organic and inorganic molecules have strong absorption lines, as shown in the Fig. 1.2 [10]. These absorption lines are due to the fundamental vibrational-rotational modes of molecular bonds. A thorough understanding of molecular structure and dynamics often involves detailed spectral analysis over a broad frequency range. Therefore, broadband lasers sources operating in the mid-infrared can be used for spectroscopy, trace gas detection and monitoring applications with high temporal and spectral resolutions.
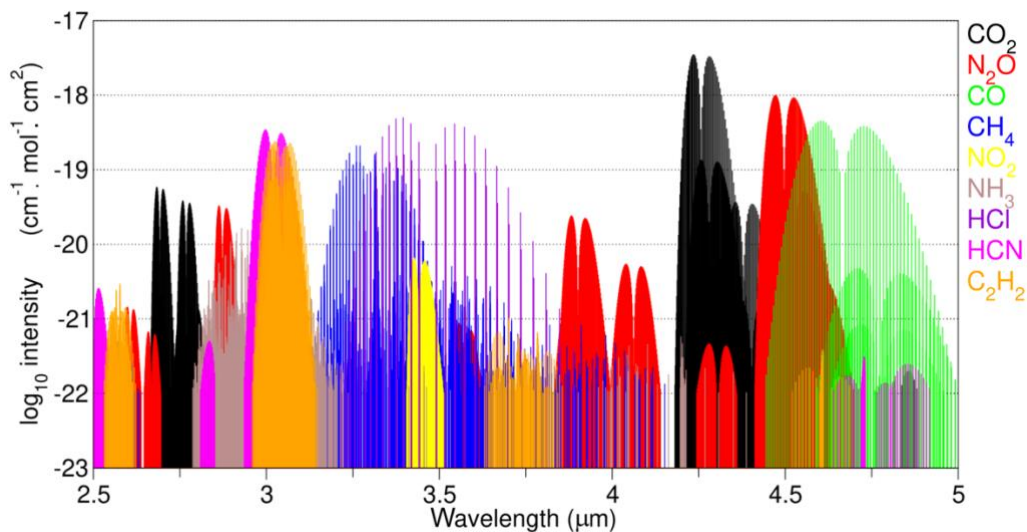
Figure 1. 2: Molecular mid-infrared fingerprints absorption line in the spectral region between 2.5 and 5 μm [2].

Laser frequency combs in the Mid-IR spectral range have been used for precise measurements of molecular structure and dynamics since the late 1990s. Frequency comb spectroscopy uses coherent combs to simultaneously provide large spectral bandwidth, high-frequency precision,

and high brightness. Using mode-locked lasers for parametric down-conversion is one of the approaches for generating MIR frequency combs [21]. Due to high sensitivity and accuracy over a broad spectral bandwidth, frequency-comb spectroscopy can identify and quantify molecular species for remote sensing and microscopy applications.

Supercontinuum generation in fluoride fiber can produce ultra-broadband spectra with high brightness, well suited for spectroscopy applications. In 2013, Weiqiang Yang, et al. [22] reported high power all fiber mid-IR supercontinuum generation in a ZBLAN fiber, covering the spectral range from 1.9 to 3.9 µm with 7.11 W average power. Consequentially, tunable ZBLAN fiber-based systems have been utilized for detection of molecular species around 3 µm. In 2018 Majewski et al. demonstrated tunable Dy-doped ZBLAN fiber laser tunable from 2.95 µm to 3µm, which covers molecular absorption of OH, NH and CH-based molecules located in Mid-IR region [23]. In 2019 Woodward et al. developed a swept-wavelength mid-infrared fiber laser, exploiting the broad emission of dysprosium, and using an acousto-optic tunable filter to achieve electronically controlled swept-wavelength operation from 2.89 µm to 3.25 µm, which is used for real-time remote sensing of ammonia gas [24].

Strong-field physics and attosecond science

Strong field physics is exploring interactions of intense electromagnetic fields with the binding electric fields of matters. Since Keldysh et al. [28] introduced a theoretical framework to characterize atomic ionization as a process that evolves with the intensity and wavelength of the fundamental field, strong field physics has developed into a mature field of research for tracking electronic and structural dynamics on the attosecond time scale. Semiclassical recollisional

model can be used to qualitatively understand strong-field interactions. The dimensionless adiabaticity parameter γ defining tunneling conditions in the model is [29]:

$$\gamma = \sqrt{\frac{I_p}{2U_p}} \sim \frac{1}{\sqrt{I}\lambda} \ll 1$$

where I_p is the ionization potential of the target atoms, $U_p \propto I\lambda^2$ is ponderomotive energy, I is the laser peak intensity, and λ is the central driving wavelength. There are many benefits when using Mid-IR laser sources instead the ubiquitous Ti:sapphire lasers working at 0.8μm [30]. First, strong field re-collisions occurring at low peak intensities has the ability to avoid appreciable ground-state depletion. Moreover, the longer-wavelength field is also beneficial for reducing the inherent limitations associated with the attosecond pulse chirp, and can generate high-quality attosecond bursts via high-harmonic generation with higher cutoff energies $(I_p + 3.2U_p \propto \lambda^2)$. Experimental demonstration by Tenio et al. in 2012 is shown in Fig.1.4 [31]. The ultrahigh harmonics (up to orders greater than 500) have been generated by guiding a 330 TW/cm^2, 3.9 μm, 80-fs pulse in high-pressure helium gas, producing a bright supercontinuum that spans the entire electromagnetic spectrum from ultraviolet to the soft x-ray region, and which corresponds to a 2.5 attosecond (single x-ray cycle) transform-limited pulse.
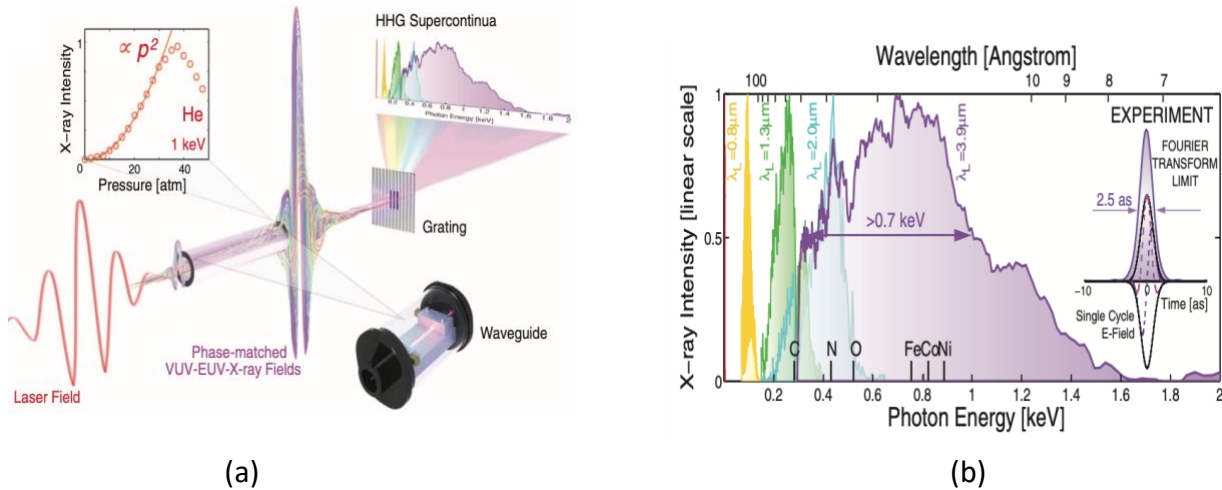
Figure 1. 3: (a) Schematic illustration of the coherent kilo–electron volt x-ray super-continua emitted when a mid-IR laser pulse is focused into a high-pressure gas-filled waveguide. (b) Fourier transform–limited pulse duration of 2.5 attoseconds.[31]

Laser-driven particle acceleration

Although the majority of laser acceleration work up to date have been done using Ti:sapphire lasers, use of mid-IR laser pulses to drive dielectric laser-accelerators can mitigate the problem of laser-induced breakdown in dielectric structures at high optical intensities, relax structure fabrication requirements, and allow greater pulse energies to be injected into the structure. In 2013, Igor Jovanovic et al. developed a robust scheme for 500μJ seed pulse generation at 5 μm using a 2mJ high-energy 2-μm pump source [32].

In laser wake-field acceleration, critical power threshold for relativistic self-focusing decreases with the increase of laser wavelength squared, and the ponderomotive force that pushes the electrons outwards and drives the Wakefield also scales as laser wavelength squared. Thus, Mid-IR sources can significantly increase accelerated charge, compared to NIR sources. First laser

plasma Wakefield acceleration driven by ultrashort mid-infrared (IR) laser pulses is reported by D. Woodbury et al. [32] using $\lambda = 3.9$ μm, 100 fs, 0.25 TW pulses, where relativistic electron acceleration up to ~12 MeV was achieved.

1.3 Current status of fluoride fiber lasers

Fiber lasers are well known for their robustness, stability, compactness, high beam quality, and high average power. Yb-doped silica fibers operating at 1μm, Yb/Er co-doped silica fibers operating at 1.55μm, and Tm-doped silica fibers operating at 2μm are relative mature technologies [34-36]. However, the longest laser wavelength from a silica fiber reported is 2.188um, due to the sharp transmission cutoff for wavelengths longer than 2.2um [8]. Fluoride-glass fibers are well suited for operation in Mid-IR. In 1975, M. Poulain et al. [37] reported the first heavy metal fluoride glass (HMFG) ZrF4-BaF2-NaF ternary system. In 1981, Shibata Shuichi et al. [38] first reported the ZBLAN glass, which is comprised of 53 mol% ZrF_4, 20 mol% BaF_2, 4 mol% LaF_3, 3 mol% AlF_3 and 20 mol% NaF. Until now, ZBLAN is still one of the most successful compositions, operating in the 2.5-4.5μm range. Since ZBLAN glasses are mainly composed of ZrF4, they are often called ZrF_4-glass fibers or ZrF_4-fibers.

Because of the low phonon energy (580 cm^{-1}) of ZBLAN glass [39] the theoretically predicted minimum loss in mid-IR is < 0.01 dB/km. Current commercial ZBLAN fibers exhibit typical background attenuation of ~10 dB/km at ~3μm, and thus there is significant potential to further reduce this loss by increasing the purity of the material. Moreover, low phonon energy enables high solubility of rare earth ions, which can reach up to 10 mol.%, thus enabling heavily doped

ZBLAN fibers. The attenuation of ZBLAN fibers (Le Verre Fluoré), compared to that of low-OH

silica fibers is shown in Fig. 1.5 [40].
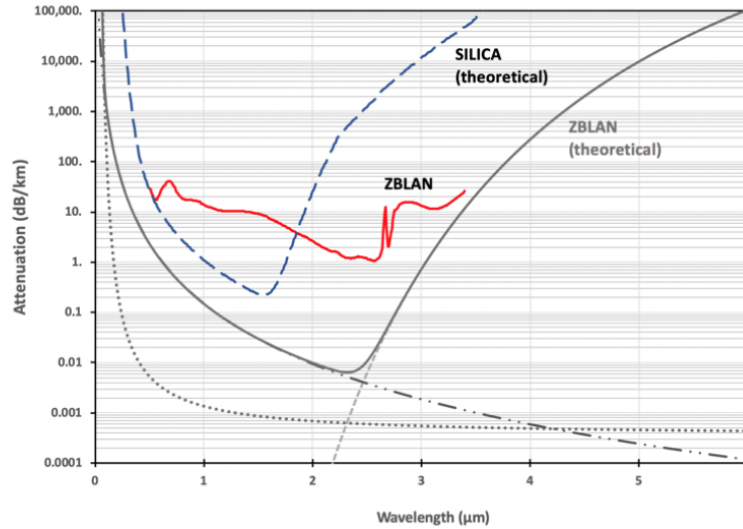
Figure 1. 4: Theoretical loss spectra for a typical ZBLAN optical fiber (solid gray line), silica
optical fiber (dashed blue line), industry best manufactured ZBLAN fiber(solid red line) as
function of wavelength (μm) [40]

In addition to ZBLAN(ZrF_4)-based fluoride fibers, InF_3 based fluoride fibers are commercially

also available for using in Mid-IR. Compared with ZBLAN, InF_3 have slightly higher glass

transition temperature (300 °C) and lower phonon energy. It is worth emphasizing that InF_3-

based fibers have availability to provide with broader spectral transmission (up to >5.5 μm) than

ZBLAN, as shown in Fig. 1.6 [41]. Also, refractive index of InF_3 is larger than that of ZBLAN.

These benefits make InF_3 fiber attractive for supercontinuum sources. In 2016 Gauthier, Jean-

Christophe, et al. reported the first InF3-based supercontinuum source with the spectrum

extending from 2.4μm to 5.4μm [42]. Since this thesis is mainly focusing on high-power, high-

energy fiber amplifier in Mid-IR region, we will further limit ourselves to discussing only

ZBLAN based fibers.
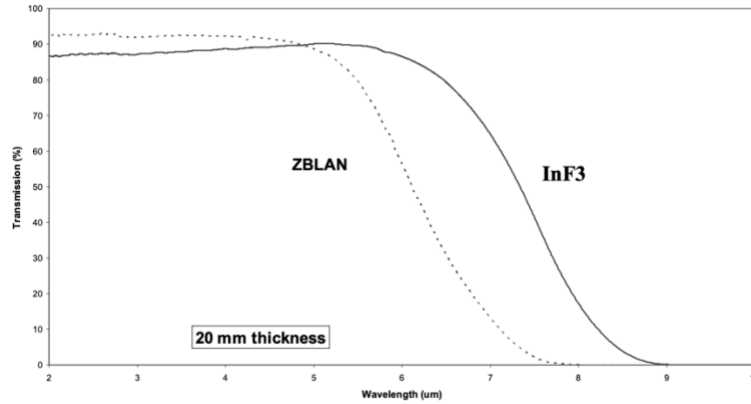
Figure 1. 5: ZBLAN (dashed line) and InF$_3$ (solid line) glasses transmission windows. [41]

AlF$_3$ fiber is well known for enhanced chemical durability and strength. The Young's Modulus 63.8 GPa of AlF$_3$ is higher than that of ZBLAN glass (52.7 GPa). The glass transition and melting temperature of AlF$_3$-based bulk glasses are 392 °C and 650 °C, respectively [43], which are almost 2 times of that of ZBLAN. Thanks to their outstanding chemical and mechanical properties, AlF$_3$ fibers are usually used as end-capps for protecting ZBLAN fiber facets in high power/energy fiber lasers systems, and also used for Er:YAG and Er:YSGG lasers as delivery fibers in medical applications.

Several rare earth ions, such as Ho^{3+}, Pr^{3+}, Dy^{3+}, Er^{3+} ,that can be doped into ZBLAN glass, can be used in fiber lasers operating at around 3 μm, as shown in Fig. 1.7. However, there is a number of significant advantages for Erbium doped ZBLAN fibers, which use $^4I_{11/2} \rightarrow {}^4I_{13/2}$ Er-ion transition for broadband gain at around 2.6-2.9 μm compared with other dopants operating at similar wavelengths. Widely available, efficient, robust and reliable telecom-grade laser diodes operating at 976nm can be used to pump this $^4I_{15/2} \rightarrow {}^4I_{13/2}$ Er transition, while e.g. Ho^{3+} needs pumping at 1.15 μm, and Dy3+ needs pumping at 1.1 μm, which are not

compatible with existing high power pump diodes. Furthermore, high concentration Er-doped (>1mol.%) ZBLAN fibers have high pumping efficiencies (up to 49.5%) due to 1-to-2 pump-to-signal photon conversion (see chapter 2), which especially important for high power lasers – up to 70W reported so far with an Er:ZBLAN fiber [44, 45].
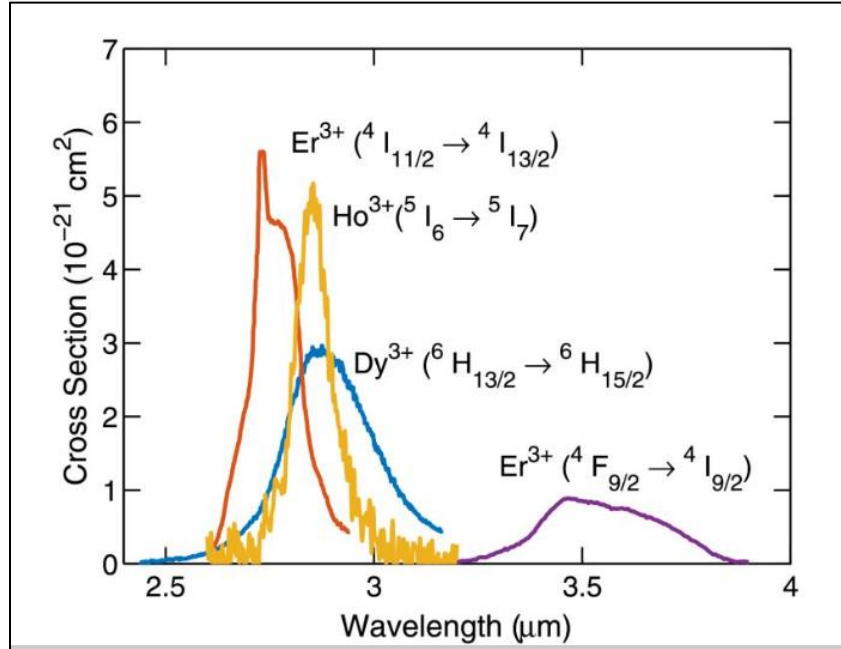
Figure 1. 6: Emission cross section for rare earth ions doping materials [41]

Table 1.1 [46] summarizes properties of ZBLAN glass with a comparison to those of silica glass. Infrared edge of ZBLAN glass is much longer than that of silica glass, but stability, chemical durability, and mechanical robustness of ZBLAN glass is much worse than those of silica glass. One of the most import problem occurring at high power in ZBLAN glass is the photo-degradation through OH diffusion, limiting fiber durability. For example, as reported in [47] Er:ZBLAN fiber laser operated without protection for less than 10h for 20W level output due to the OH-diffusion. Furthermore, laser induced damage threshold at air-glass surface (always

lower than glass bulk damage threshold) is the other limitation for high power lasers. As reported in [48] measured ZBLAN fiber damage threshold of ~3GW/cm^2 for 10-ns pulses at 2.8µm is much lower than 475GW/cm^2 measured in fused silica using 7.5ns pulses at 1.064µm [49]. To mitigate these issues, it is necessary to use highly stable material spliced as an endcap at each end of the fiber to protect ZBLAN fiber tips from OH diffusion, and to significantly improve laser operation lifetime. Additionally, endcaps also allow expansion of the output beam to lower the beam intensity at the output interface to below glass damage threshold [50].

Glass property	Silica	ZBLAN
Approximate transmission range (1 mm thickness, $T > 10\%$) (µm)	0.16–4.0	0.22–8.0
Maximum phonon energy (cm^{-1})	1100	600
Transition temperature (°C)	1175	260
Specific heat (J/(g·K))	0.179	0.151
Thermal conductivity, W/(m·K)	1.38	0.628
Expansion coefficient (10^{-6}/K)	0.55	17.2
Density (g/cm^3)	2.20	4.33
Knoop hardness (kg/mm^2)	600	225
Fracture toughness (MPam$^{1/2}$)	0.72	0.32
Poisson's ratio	0.17	0.17
Young's modulus (Gpa)	70	58.3
Shear's modulus (Gpa)	31.2	20.5
Bulk's modulus (Gpa)	36.7	47.7
Refractive index (@ 0.589 um)	1.458	1.499
Abbe number	68	76
Zero material dispersion wavelength (µm)	1.3	1.6
Nonlinear index (10^{-13} esu)	1	0.85
Thermo-optic coefficient (10^{-6}/K)	11.9	−14.75

Table 1. 1: Comparison of basic properties between silica and ZBLAN glasses [37]

Different glass materials,suchas AlF$_3$, GeO$_2$, SiO$_2$, Al$_2$O$_3$ can be used as endcaps for protecting the ZBALN fibers. AlF$_3$ appears to be the best endcapping solution for the ~3µm high-power lasers. The refraction index of AlF$_3$ (n_{AlF3} = 1.46 [51]) is close to that of the ZBLAN glass (n_{ZBLAN} = 1.48 [52]), thus effectively reducing Fresnel reflections at the joint between the two materials in an endcap, therefore avoiding the internal lasing in high power amplifier systems. Moreover, the mechanical and chemical prosperities of AlF$_3$ are much better than ZBLAN glass

[50], thus they can protect ZBLAN fibers from OH-diffusion induced degradation and intense laser induced optical damage.

Before the splicing procedure, the clean and flat facet of fibers need to be cleaved shown in Fig. 1.8 (a). The cleaver we used is Vytran LDC401A. Different from the fused silica fiber cleaving, the soft glass fiber needs to be straightened thermally, and use of micro-backstop is also necessary to reduce the offset and vibrations during the straight cleaving. Due to the low transition temperature of ZBLAN and AlF_3 glasses Iridium filament splicer (Vytran LFS4000), working robustly at low powers, must be used fluoride fiber splicing. The splicer has the offset shown in Fig. 1.8(a), necessary due to the significant transition temperature and chemical composition difference and between ZBLAN and AlF_3 (260 °C for fluoride, 390 °C for AlF_3). During splicing procedure, AlF_3 fiber can be pushed in a controlled manner into sufficiently heated ZBLAN fibers, using an optimized splicing program with respect to the offset, gap distance between two fiber facets, and other aplicing parameters. With this technology a permanent and robust joint can be created as shown in Fig. 1.8 (b). The AlF_3 usually needs to be polished or cleaved at an angle to avoid internal lasing, as illustrated in Fig. 1.8 (c). The single mode laser output beam in Fig. 1.8(d) indicates the distortion-free interface between the fiber and endcap glasses.
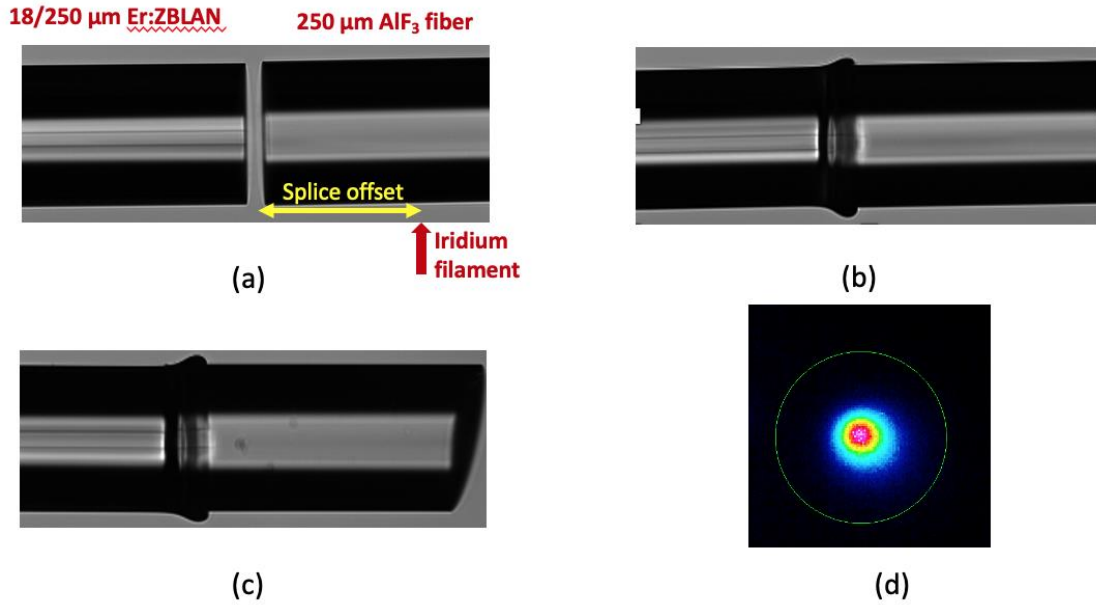
Figure 1. 7: Photographs of (a) clean and flat fiber facet of 18/250µm Er:ZBLAN (left) and 250µm AlF$_3$ (right). The iridium filament offset has also been shown; (b) Robust endcaps of ZBLAN and AlF$_3$; (c) 12° angle polished endcaps; (d) Undistorted laser output beam from active ZBLAN fiber for endcap testing.

1.4 Objective and motivation

Objective of thesis is to validate feasibility of high-power and energy short pulse fiber-based sources in the mid-IR spectral range. Such sources by themselves have numerous interesting applications in this spectral range (see chapter 1.2). Mid-IR source development is closely linked to the ongoing work on efficient parametric frequency down conversion into LW-IR spectral range [25,27,88]. Fig. 1.9 shows the key aspects of the envisioned Fiber Laser-based Sources of TW Peak Power Ultrashort Pulses at 10-12µm. High energy fiber based mid-IR sources under development are intended to be pump and, seed sources for LWIR OPCPA. This thesis is focusing on the initial steps of the whole project, and explores high energy generation potential

with Er:ZBLAN fibers. This is also intended to serve as a basis for future Fiber CPA systems and coherent combining work.
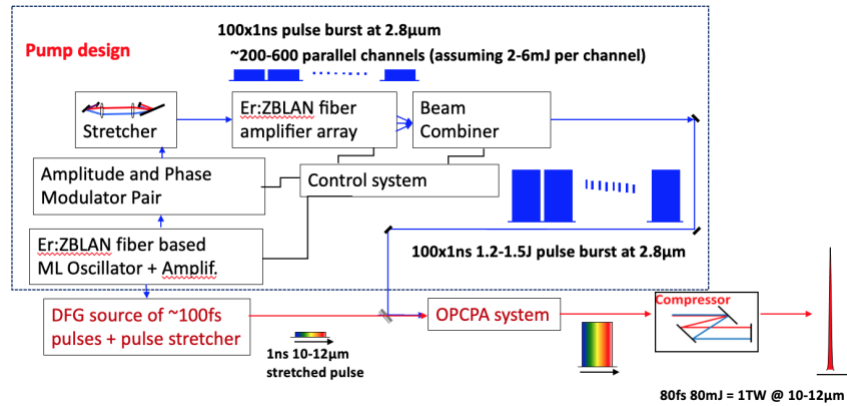
Figure 1. 8: Key aspects of Fiber Laser-based Sources of TW Peak Power Ultrashort Pulses at 10-12µm

Chapter 2 Modeling of High Energy Er:ZBLAN Fiber Amplification

2.1 Abstract

Numerical model of erbium-doped fluoride fiber amplifier is presented in this chapter. Using this model we simulated 30µm-core and 50µm-core Er:ZBLAN fiber amplifiers, and compared the calculated results with the experimental data to calibrate this model. This model can predict the stored energy of the fiber amplifier, which can help guiding the high-energy fiber laser experiments.

2.2 Background and introduction

Erbium is a common doping element widely used in fused silica fibers to provide gain at around 1.55µm for optical telecommunications [53]. However, Erbium doped fluoride glass fibers operating at around ~2.8µm is a relatively new gain medium which had attracted significant recent research efforts [54-60]. Numerical and theoretical analysis is important to gain insight

into Er^{3+} doped fluoride glass fiber operation at ~2.8µm, which is very useful to guide laser system design and experimental implementation. In this chapter, section 2.3 describes Erbium ions energy level structure in ZBLAN glass fibers, and the three methods used to overcome "bottlenecking" of the 2.8µm transition: Er^{3+} and Pr^{3+} co-doping [54-56], cascading ot 1.55µm and 2.8µm transitions in Er^{3+} [58-61], and energy transfer upconversion (ETU) in heavily doped Er^{3+} [62-65] fluoride fiber lasers; and section 2.4 formulates the rate equations for heavily doped Er:ZBLAN fibers. These rate equations are much more complicated than traditional three level systems, since they have to include the energy transfer up-conversion (ETU) processes. Section 2.5 presents fiber amplifier modeling results after including light propagation equations as well as proper boundary conditions. This model can consider continuous-wave (CW) as well as pulsed lasers and amplifiers. Different from the previously published simulation and modeling results for Er:ZBLAN fibers, we added the amplified spontaneous emission (ASE) terms to the terms describing pump and signal propagation. These equations are solved using shooting method to resolve the boundary value problems (BVPs). Section 2.6 presents model calibration and parameter tuning using experimentally measured small signal gain. With this calibrated model we describe Er:ZBLAN fiber amplifiers quantitively, predicting stored energies in 30-µm and 50-µm core Er:ZBLAN fiber amplifiers that were used in subsequently described experiments.

2.3 Er^{3+} energy levels in ZBLAN glass

Fig. 2.1 shows the energy levels of Er^{3+} ions in ZBLAN glass fibers. Ground state absorption of 976nm pump excites Er^{3+} into $^4I_{11/2}$ level, and the relevant laser transition at 2.8µm occurs

18

between $^4I_{11/2}$ and $^4I_{13/2}$ levels. However, the lifetime of the upper laser level ($^4I_{11/2}$) is 6.9ms, which is smaller than that of the lower laser level ($^4I_{11/2}$) in this three-level laser system (which is 9ms). Consequentially this "bottlenecks" the 2.8µm transition, leading to 1.55µm lasing occurring between $^4I_{13/2}$ and $^4I_{15/2}$ levels. There are three ways to mitigate this population bottleneck.
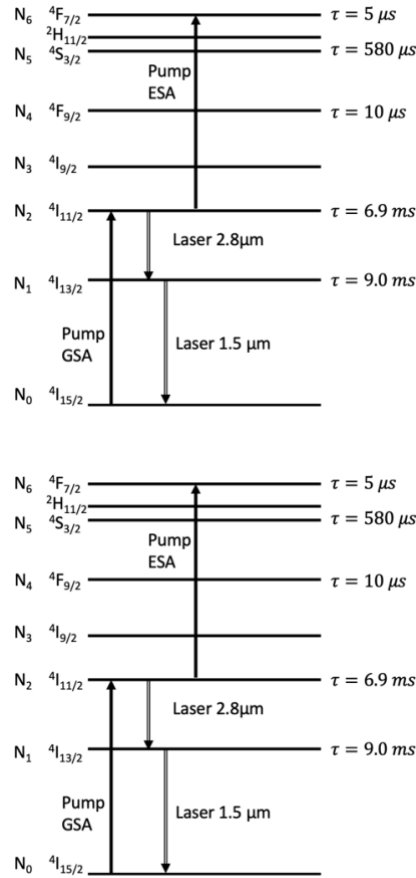
Figure 2. 1: Energy levels diagram of Erbium ions in ZBLAN glass. 2.8µm transition is $^4I_{11/2} \longrightarrow {}^4I_{13/2}$, and 1.55µm transition is $^4I_{13/2} \longrightarrow {}^4I_{15/2}$

First is that Er^{3+} and Pr^{3+} co-doping in ZBLAN glass fiber can be used to avoid this population bottlenecking [54]. The energy level diagram of Er^{3+} and Pr^{3+} in ZBLAN is shown in Fig. 2.2. The Er^{3+} ion excitation energy caused by the GSA of 790nm pump into the level $^4I_{9/2}$ can transfer

to the $^1G_4$ level of Pr^{3+} , while the energy of the Er^{3+} ions which decayed into the $^4I_{13/2}$ level can transfer to the $^3F_3$ level of Pr^{3+}. These excited states of Pr^{3+} will decay to the ground state by fast non-radiative relaxation. Measurements reported in [57] indicate that the energy transfer (ET) from $^4I_{11/2}$ is significantly slower than that of the ET from the level $^4I_{13/2}$. Therefore, this last ET process can de-sensitize the lower laser level of the 2.8µm transition. Thus, the Er^{3+} and Pr^{3+} co-doped ZBLAN fiber laser simplifies to the traditional four-level laser system. The drawback of this method is that it causes significant heating, since most of the pumping energy is wasted by the non-radiative relaxation processes in Pr^{3+}.
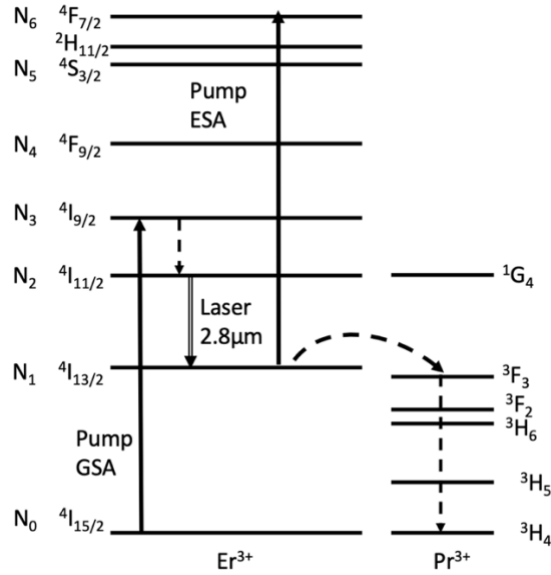
Figure 2. 2: Energy level diagram of Er^{3+} and Pr^{3+} ions in ZBLAN glass, indicating the processes that are relevant for the operation of high-power diode pumped Pr^{3+}-codoped Er^{3+} fiber lasers operating at the transition $^4I_{11/2} \longrightarrow {}^4I_{13/2}$. GSA is the ground state absorption. ESA is the excited state absorption.

Another way to de-excite the $^4I_{13/2}$ level is to cascade the 2.8 µm laser transition simultaneously with 1.55 µm transition in low-doped Er laser to mitigate the population bottlenecking. The

relevant details of the energy level diagram is shown in Fig. 2.3. The GSA at 976 nm is used to pump the fiber laser. The laser can be built forming the oscillator cavity for both the 2.75µm, occuring between $^4I_{11/2}$ and $^4I_{13/2}$ levels, and the 1.55µm, occuring between $^4I_{13/2}$ and $^4I_{15/2}$ levels, signals. The radiation at 1.55µm can deplete the ion population in the $^4I_{13/2}$ level, thus decreasing the lifetime of the lower 2.8µm laser level. However, this cascaded Er^{3+} doped fiber laser scheme is not suitable for high power generation in double-clad fibers, since it requires large pump irradiances, and hence is more suitable for core pumped fiber lasers whose pump power is limited.
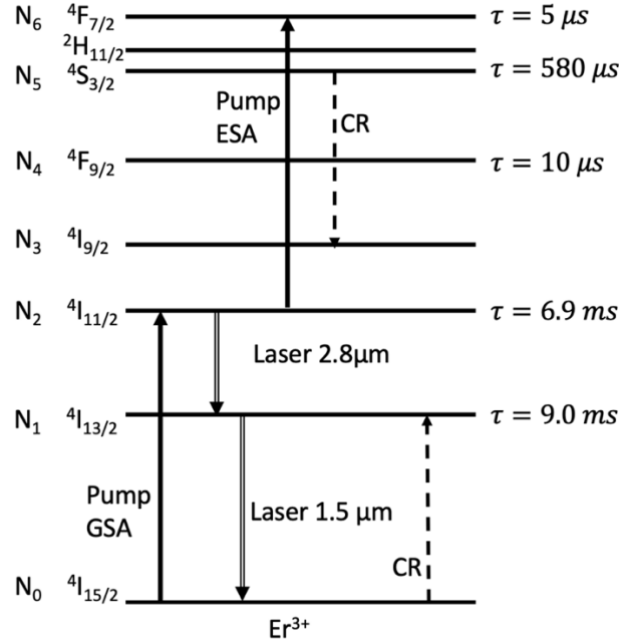
Figure 2. 3: Simplified energy level diagram of Er3+ showing the pump and laser transitions (left-hand side) in the cascade regime as well as potential parasitic processes (right-hand side) that can lead to additional heat generation. [58]

The most effective method, which is also compatible with high power generation, is to utilize the heavy doping of Er^{3+} (usually larger than 6 mol.%) in ZBLAN glass to remove the ~2.8µm laser

transition bottleneck through energy transfer up-conversion (ETU) processes [66,67]. ETU processes occur in the upper and lower lasing levels as shown in Fig. 2.4. As shown in Fig. 2.4, ETU_1 reduces the population in the lower laser level $^4I_{13/2}$ by transferring excitation energy of one ion to the higher level $^4I_{9/2}$ and the excitation energy of a second ion to the ground level $^4I_{15/2}$, thus reducing the bottlenecking of the lower laser level $^4I_{13/2}$. Simultaneously ETU_2 also occurs reducing the population in the upper laser level $^4I_{11/2}$, which is not useful. As reported in [68], the measured ETU_1 rate of 3.6×10^{23} m^3s^{-1} is significantly larger than measured ETU_2 rate of 1.2×10^{23} m^3s^{-1}. Therefore, the useful ETU_1 process is the dominant one. Since the ETU process is proportional to the erbium ions concentration, the population bottlenecking can be effectively removed by using heavy doping of Er^{3+} ions. Furthermore, the ETU process allows a recycling of the excitation, because half of the excited ions is upconverted to the higher $^4I_{9/2}$ level, decay from which populates the upper laser level again. This can enhance the quantum efficiency by a factor of two, and slope efficiencies of up to 50% which exceed the Stokes efficiency of 35% were demonstrated experimentally [44]. In this thesis work we use only the heavily doped Er^{3+} ZBLAN fiber lasers and amplifiers.
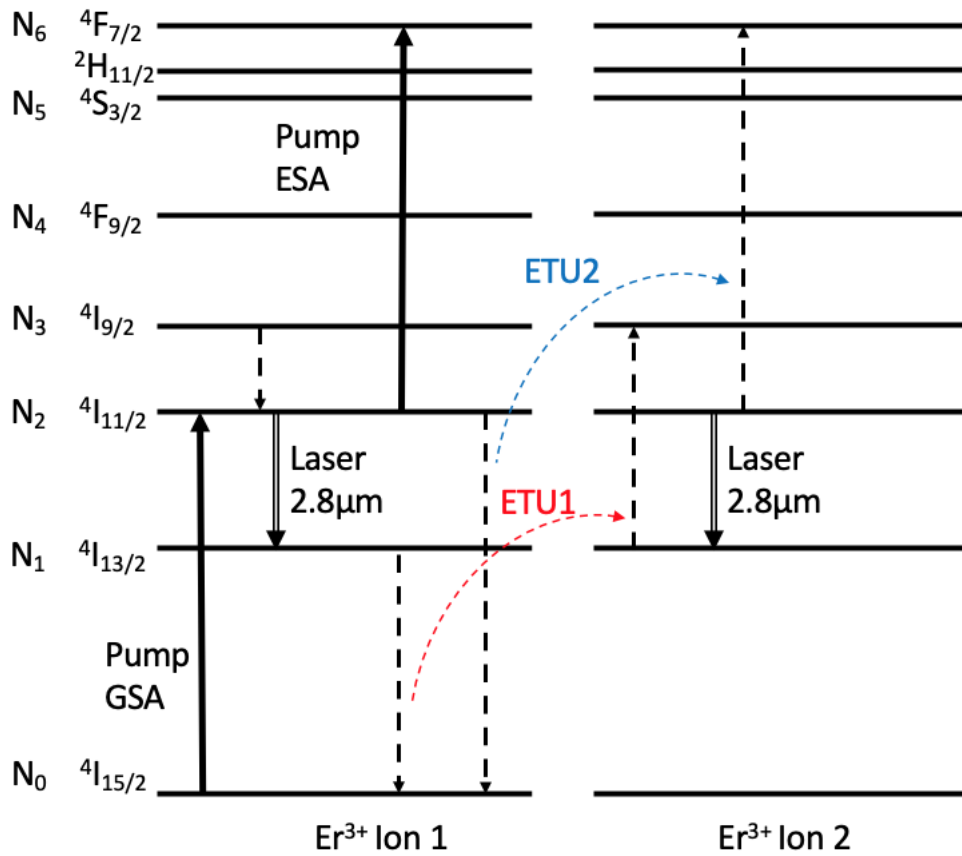
Figure 2. 4: Schematic diagram of energy levels of heavily erbium doped ZBLAN fiber lasers, and the energy transfer up-conversion (ETU) processes between two erbium ions.

2.4 Rate equations for Er:ZBLAN fiber laser

According to the energy level diagrams of heavily erbium doped ZBLAN fiber shown in Fig.2.4, the rate equations for the population densities at each energy level N_i are given by [67]:

$$\frac{dN_6(z,t)}{dt} = R_{ESA}(z,t) - \tau_6^{-1}N_6(z,t) + W_{22}N_2^2(z,t) \qquad (2.1)$$

$$\frac{dN_5(z,t)}{dt} = \beta_{65}\tau_6^{-1}N_6(z,t) - \tau_5^{-1}N_5(z,t) - W_{50}N_5(z,t)N_0(z,t) \qquad (2.2)$$

$$\frac{dN_4(z,t)}{dt} = \sum_{i=5,6}[\beta_{i4}\tau_i^{-1}N_i(z,t)] - \tau_4^{-1}N_4(z,t) \qquad (2.3)$$

$$\frac{dN_3(z,t)}{dt} = \sum_{i=4,..,6}[\beta_{i3}\tau_i^{-1}N_i(z,t)] + W_{50}N_5(z,t)N_0(z,t)$$
$$+W_{11}N_1^2(z,t) - \tau_4^{-1}N_4(z,t)$$
$$\qquad (2.4)$$

$$\frac{dN_2(z,t)}{dt} = R_{GSA}(z,t) - R_{ESA}(z,t) + \sum_{i=3,..,6}[\beta_{i2}\tau_i^{-1}N_i(z,t)]$$
$$-R_{SE}(z,t) - \tau_2^{-1}N_4(z,t) - 2W_{22}N_2^2(z,t)$$
$$\qquad (2.5)$$

$$\frac{dN_1(z,t)}{dt} = \sum_{i=2,..,6}[\beta_{i1}\tau_i^{-1}N_i(z,t)] - \tau_1^{-1}N_1(z,t) + W_{50}N_5(z,t)N_0(z,t)$$
$$- 2W_{11}N_2^2(z,t) + R_{SE}(z,t)$$
$$\qquad (2.6)$$

$$N_{tot} = \sum_{i=0,..,6} N_i(t) \qquad (2.7)$$

Here N_i is the ion population density of ith energy level. Variables z and t are used to account for the population density changes along the fibers over time. The τ_i is the intrinsic lifetime of ith energy level in the system at low doping concentrations, including radiative and multi-phonon relaxations. W_{ij} describes the energy transfer up-conversions process of two ions between the levels i and j. W_{11} and W_{22} represent the ETU1 and ETU2 transition rates from the lower ($^4I_{13/2}$) and the higher ($^4I_{11/2}$) lasing energy levels of the ~2.8μm transition respectively. W_{50} represents

the cross relaxation (CR) parameter from the thermally coupled $^4S_{3/2}$, $^2H_{11/2}$ energy levels. β_{ij} are the branching ratios, describing the probability of ions decaying from level i into level j.

The R_{GSA} and R_{ESA} stands for the pumping rates of the ground state absorption (GSA), and of the excited state absorption (ESA) defined as:

$$R_{GSA}(z,t) = \frac{\lambda_p \gamma_p \sigma_{GSA}(\lambda_p)}{hcA_{eff}} N_0(z,t)[P_p^+(z,t) + P_p^-(z,t)] \tag{2.8}$$

$$R_{ESA}(z,t) = \frac{\lambda_p \gamma_p \sigma_{ESA}(\lambda_p)}{hcA_{eff}} N_2(z,t)[P_p^+(z,t) + P_p^-(z,t)] \tag{2.9}$$

Here λ_p denotes the pump wavelength of 976nm, h is the Planck constant ,and c is the speed of light. σGSA and σESA are the GSA and ESA cross sections at the pump wavelength, respectively. Fig. 2.5 shows the typical GSA and ESA cross sections of Er^{3+} vs wavelength, measured at room temperature.
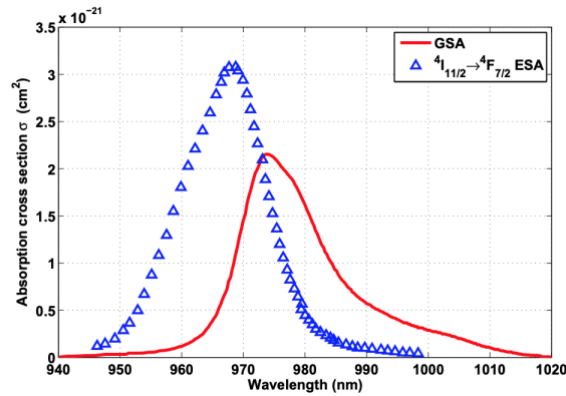
Figure 2. 5: Measured cross sections of ground state absorption (GSA) and excited state absorption (ESA) for Er:ZBLAN around 980nm [69]

A_{eff} represents the effective mode area for the fiber core. $P_p^+(z,t)$ and $P_p^-(z,t)$ are the forward and backward propagating pump powers, respectively. The overlap factor γ_p is calculated from the ratio of fiber core area and fiber pump cladding area of a double-clad fiber. R_{SE} stands for the spontaneous emission from the laser transition given by:

$$R_{SE}(z,t) = \frac{\lambda_s \gamma_s \sigma_{SE}(\lambda_s)}{hcA_{eff}} [b_2 N_2(z,t) - \frac{g_2}{g_1} b_1 N_1(z,t)] [P_s^+(z,t) + P_s^-(z,t)] \qquad (2.10)$$

where λ_s denotes the signal (laser) wavelength. Overlapping factor γ_s denotes the power filling

$$(2.11)$$

factor for the signal. Assuming the fiber core area is uniformly doped by Er^{3+} within the core radius r_{core} , the doping concentration as a function of radius is given by:

$$\rho(r) = \begin{cases} \rho_0 & \text{If } r \leq r_{core} \\ 0 & \text{otherwise} \end{cases}$$

The power filling overlap factor for the signal γ_s between the doping and a specific mode can is defined as:

$$\gamma_s = 1 - e^{-2(\frac{r_{core}}{\omega_0})^2} \qquad (2.12)$$

Here ω_0 is the mode field radius, given by:

$$\omega_0 = 0.65 + 1.619V^{-1.5} + 2.876V^{-6} \qquad (2.13)$$

where V is the normalized frequency. σ_{SE} is the emission cross-section, whose dependence on the wavelength is shown in Fig. 2.6 [70]. b$_1$ and b$_2$ are Boltzmann factors for the ^{4}I$_{13/2}$ and ^{4}I$_{11/2}$ laser levels. $g_2 = g_1 = 2$ are Kramers' degeneracies [67]. $P_s^+(z,t)$ and $P_s^-(z,t)$ denote forward (moving in the same direction as the pump) and backward (moving in the opposite direction as the pump) signal powers along the z axis, respectively.
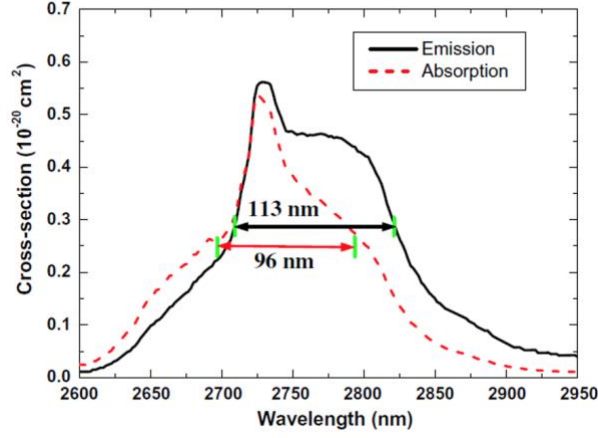
Figure 2. 6: Emission cross section for $^4I_{11/2} \longrightarrow {}^4I_{13/2}$ (solid line), excited-state absorption cross section for $^4I_{13/2} \longrightarrow {}^4I_{11/2}$ (dashed line). The line with two arrows indicates the full width at half-maximum (FWHM) [70]

2.5 Er:ZBLAN fiber amplification model

In continuous wave region, the power evaluation of the pump light along the fiber is shown to be:

$$\pm \frac{dp_p^\pm(z)}{dz} = -\gamma_p[\sigma_{GSA}N_0(z) - \sigma_{ESA}N_2(z)] \times p_p^\pm(z) - \alpha_p p_p^\pm(z) \qquad (2.14)$$

where α_p represent the background loss coefficients of pump light. For the signal propagation in amplifier system, the amplified spontaneous emission (ASE) must be considered. ASE is the most important factor, since it depletes the population in the laser upper level, therefore limiting the stored energy. The source of ASE is spontaneous emission (SE), by which an atom, molecule, or ion in an excited state decays to a lower-energy state, resulting in the creation of a photon. If the SE happens in the gain fiber, a fraction of the photons emitted is coupled into fiber

modes, and tis hen amplified while propagating along the fiber. The number of photons that are coupled into fiber modes is given by [71]:

$$dn(v) = 2hvdv\sigma_e(v)n_2\Gamma_k = 2\Gamma_k\,\sigma_e(\lambda)n_2\frac{hc^2}{\lambda_k^3}\Delta\lambda \qquad (2.15)$$

The signal and ASE light evaluation equation is given by:

$$\pm\frac{dp_s^\pm(z)}{dz} = -\gamma_s\sigma_{SE}\left[b_2N_1(z)\,-\left(\frac{g_2}{g_1}\right)b_1N_2(z)\right]\times p_s^\pm(z)$$
$$-\alpha_sp_s^\pm(z) + 2\sigma_{SE}N_2(z)\frac{hc^3}{\lambda_s^3}\Delta\lambda \qquad (2.16)$$

where α_s is the background loss coefficient for the signal. The pump power and signal power at the fiber ends are limited by the boundary conditions shown in Figure 2.7.
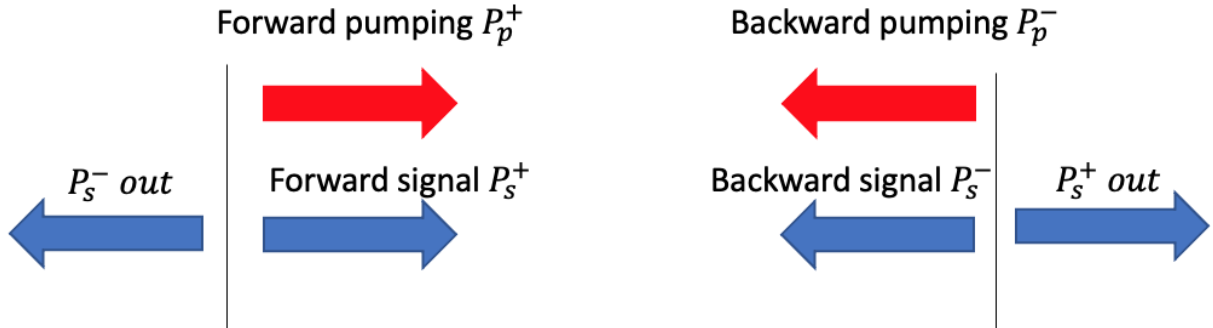
Figure 2. 7: Boundary conditions at the fiber ends. P_p^+ is the forward pump power; P_s^+ is the forward seed power; P_p^- is the backward pump power; P_s^- is the backward seed power.

The original rate equations (2.1) - (2.7) include all 6 energy-levels. For simplicity, we only consider bottom three levels ($^4I_{15/2}$, $^4I_{13/2}$ and $^4I_{11/2}$). The reason is that the lifetime (~μs) of the upper levels is much smaller than that of the bottom laser energy levels (~ms). Moreover, the cross relaxation and energy transfer up-conversion (ETU) from different energy levels have been

included in parameters W_{11} and W_{22}. The other terms are responsible for non-radiative relaxations wasted by thermal effects.

The rate equation ODEs (2.14) and (2.16) are solved numerically using the Runge–Kutta method [72] within the range from z = 0 to z = L. However, for backward propagating pump and signal boundary values are known at z = L, not at z = 0. The shooting method [73] can be utilized here to solve this type of boundary value problems (BVPs). The idea is to transfer the BVPs to initial value problems (IVPs). The equation sequence begins with an initial guess for the boundary value (E.g., $p_p^-(z)$ = guessing backward pump power through). Then, the output power at z=L resulting from this "guess" initial value need to be calculated, and compared to its original boundary value. By trial and error, the initial guessing value is improved until the boundary conditions are matched.

The analysis is similar for pulsed fiber amplifiers, but numerical modeling must deal with both temporal and spatial domains for pump, signal, and ASE power evolution equations, which is given by:

$$\pm \frac{\partial p_p^{\pm}(z,t)}{\partial z} + \frac{1}{V_p} \frac{\partial p_p^{\pm}(z,t)}{\partial t} = -\gamma_p [\sigma_{GSA} N_0(z,t) - \sigma_{ESA} N_2(z,t)] \times p_p^{\pm}(z,t)$$
$$-\alpha_p p_p^{\pm}(z,t)$$

$$(2.17)$$

$$\pm \frac{\partial p_s^{\pm}(z,t)}{\partial z} + \frac{1}{V_s} \frac{\partial p_s^{\pm}(z,t)}{\partial t} = -\gamma_s \sigma_{SE} \left[b_2 N_1(z,t) - \left(\frac{g_2}{g_1}\right) b_1 N_2(z,t) \right] \times p_s^{\pm}(z,t)$$
$$-\alpha_s p_s^{\pm}(z,t) + 2\sigma_{SE} N_2(z,t) \frac{hc^3}{\lambda_s^3} \Delta\lambda$$

$$(2.18)$$

$$\pm \frac{\partial p_{ase}^{\pm}(z,t)}{\partial z} + \frac{1}{V_{ase}} \frac{\partial p_{ase}^{\pm}(z,t)}{\partial t} = -\gamma_s \sigma_{SE} \left[b_2 N_1(z,t) - \left(\frac{g_2}{g_1}\right) b_1 N_2(z,t) \right] \times p_{ase}^{\pm}(z,t)$$
$$-\alpha_s p_{ase}^{\pm}(z,t) + 2\sigma_{SE} N_2(z,t) \frac{hc^3}{\lambda_s^3} \Delta\lambda \tag{2.19}$$

Comparing with the CW analysis, the ODE is transformed into the partial differential equations (PDEs). To solve these equations, we need to know the initial pump power at the ends of fibers and the signal input pulses energy as the time progress. The boundary conditions are shown below:

Pump: $\quad p_p^+(0) = P_1 \qquad p_p^+(L) = P_2$

Signal: $\quad p_s^+(0,t) = p_{in}(t) \qquad p_s^+(L,t) = 0$

ASE: $\quad p_{ase}^+(0,t) = 0 \qquad p_{ase}^-(L,t) = 0 \tag{2.20}$

We use the finite difference methods to approximate the solution of the partial differency equations. The idea is to lay down a grid of the independent variables, and discretize the PDEs. Thus continuous-value problem is changed into a discrete-value problem consisting of a finite number of equations [73]. Both time and spatial domains are discretized into the points as shown in Fig. 2.8. Let M and N be the total number of steps in the z and t directions, and let h = L/M and k = T /N be the step sizes in the z and t directions. A small value of h and k is necessary to minimize the truncation errors, which is the fundamental error of the finite-difference approximation. However, the small step size increases computational speed proportionally with the number of steps. Therefore, h size should be chosen carefully, accounting for specific computational conditions, and the required error magnitudes.
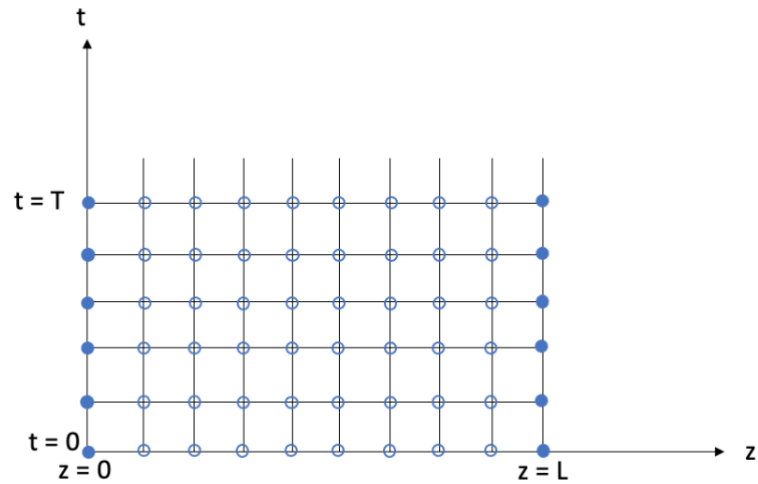
Figure 2. 8: Mesh of the finite different method. The filled blue circles represent known initial and boundary value; the open circles represent unknow value needed to be determined.

To solve this PDEs, the shooting method must be implemented similarly to the CW case. A sequence of IVPs is produced via the guessing. Then these IVPs are solved and compared with the initial boundary value. By trial and error, the initial guess is improved until the boundary value is matched.

2.6 Model calibration and prediction

In the experiment, two different fibers are used: 1.9m 30µm-core-diameter and 3.2m 50µm-core-diameter Er:ZBLAN fibers. The mode field diameters are 26µm and 37µm calculated using equation (2.13), respectively. The parameters used in the rate equations are shown in table 2.1 [67]:

Parameters	Value
τ_1, τ_2 [ms]	9.0, 6.9
τ_3, τ_4, τ_5 [μs]	10, 120, 570
β_{21}, β_{20}	0.37, 0.63
$\beta_{32}, \beta_{31}, \beta_{30}$	0.99, 0, 0.01
$\beta_{43}, \beta_{42}, \beta_{41}, \beta_{40}$	0.85, 0.006, 0.004, 0.14
$\beta_{54}, \beta_{53}, \beta_{52}, \beta_{51}, \beta_{50}$	0.34, 0.012, 0.015, 0.18, 0.44

Table 2. 1: typical values of intrinsic lifetime τ_i and branching ratios β_{ij}

The established energy transfer (ET) parameters for different doping concentration were measured in bulk ZBLAN glass in [74] as shown in the table 2.2, which is on the order of magnitude of 10^{-23} m^3/s. That is named as "strongly interacting" (SI) parameters. In 2011, Gorjan et al [68] introduced the "weakly interacting" (WI) approach, and later in 2012, it was extended by Stuart Stuart D. Jackson [67]. The WI approach assert that the rates of the interionic energy transfer processes in Er^{3+}-doped fluoride fibers may be much weaker compared to the measured rates taken from bulk glasses. The WI parameters were measured by Gorjan through fitting the experimental data to a set of equations. The common WI parameters are shown in table 2.2.

	parameter	value						
Er^{3+} Concen-tration	mol.%	0.25	1	1.22	1.7	6	5	8.75
	$ions/m^3$ [x10^{26}]	0.4	1.6	1.96	2.7	6.4	8	14
SI	W_{50} W_{11} ×10^{-23} m^3/s W_{22}	0.6	0.48 1.3 0.16	0.6 1.3 0.2	0.8 1.4 0.3	1.9 2.2 0.8	2.4 2.8 1.0	3.3 6.7 1.9
WI	W_{50} W_{11} ×10^{-24} m^3/s W_{22}		0.1 0.4 0.08	0.12 0.4 0.09	0.17 0.4 0.1	0.38 0.6 0.2	0.46 0.8 0.26	0.6 1.8 0.43

Table 2. 2: Macroscopic known energy transfer parameters in Er^{3+}: ZBLAN for different doping concentrations. Parameters from two regimes are included: strongly interacting (SI) and weakly interacting parameters (WI).

However, not all the parameters are measured directly. For example, the ESA cross-section σ_{37} and the stimulated emission cross section σ_{32} are indirectly determined from spectroscopic measurements using the JuddOfelt and McCumber theories [60]. The parameters have the tuning range used in the simulations as shown in the table 2.3.

Parameters	Typical value	Range	Tuned Value
σ_{37} (10^{-25} m^2)	1.1	0.0-2.0	1.0
σ_{32} (10^{-25} m^2)	4.5	0.5-5.7	3.6
b_2	0.113	0.1-0.2	0.06
b_3	0.2	0.1-0.2	0.2
W_{22}(10^{-23} m^3/s)	0.8	0.0-0.8	0.3

Table 2. 3: Typical indirectly measured variable parameters and the ranges used in the simulations.

Also, the WI ETU parameters varies with the doping level. There is no specific value for the 6 mol.%. In our simulation, thus, we tweaked these parameters to achieve agreement between the

model predicted small signal gain and the experimental data (see chapter 4.5), as is shown in Fig. 2.9, The tuned parameters are shown in last column in table 2.3.
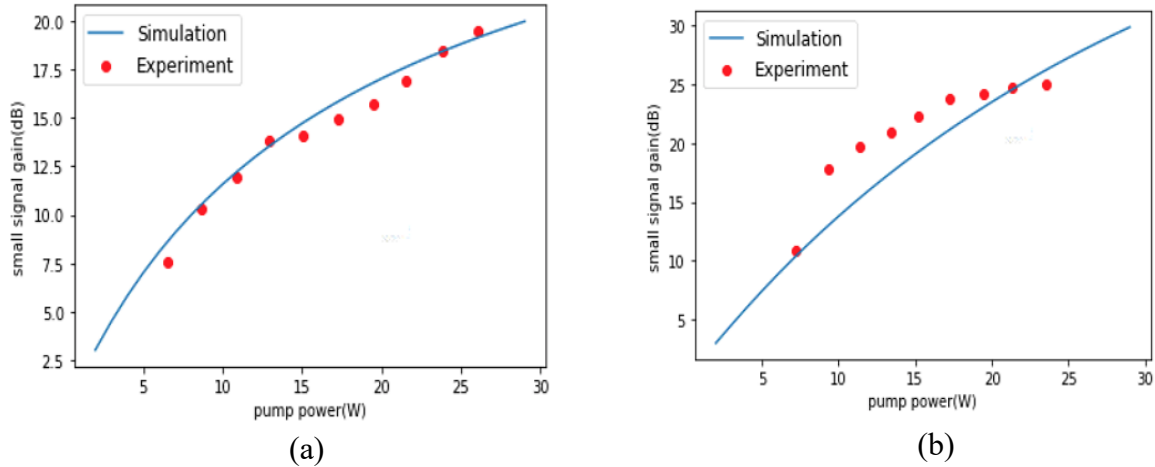
Figure 2. 9: Comparison of small signal gain of the experimental data (red dots) and the simulated data (blue line) for (a) 30-µm-core-diameter and (b) 50-µm-core-diameter Er:ZBLAN fiber amplifier

The specific fiber parameters used in the model are 3.2 m length, the core size 50µm, the mode field diameter 34µm (for 0.12 NA core), and the Er^{3+} doping concentration is 6 mol%. 20W from the 976nm pump laser is evenly split to pump the amplifier through the two ends of the fiber. The pump evolution along the fiber is shown in Fig. 2.10 (a), and the amplified spontaneous emission (ASE) in Fig 2.10 (b). Fig. 2.10 (c) shows the ion population densities along the fiber, indicating population inversion distribution along the fibers. However, because this fiber is heavily doped, the pump is highly absorbed at the both ends of the fiber, thus population inversion (N_2-N_1) at each end is much larger than that in the middle of the fiber. Time variation of the population densities in the level 1, level 2 and level 3 respectively are shown in Fig. 2.10 (d), indicating the gain recovery time of approximately 1-2ms at 20W pumping, which is consistent with the experimentally demonstrated values reported in Chapter 4.5. This suggests

that for the maximum energy extraction pulse repetition rate should not exceed 500Hz to 1kHz range.
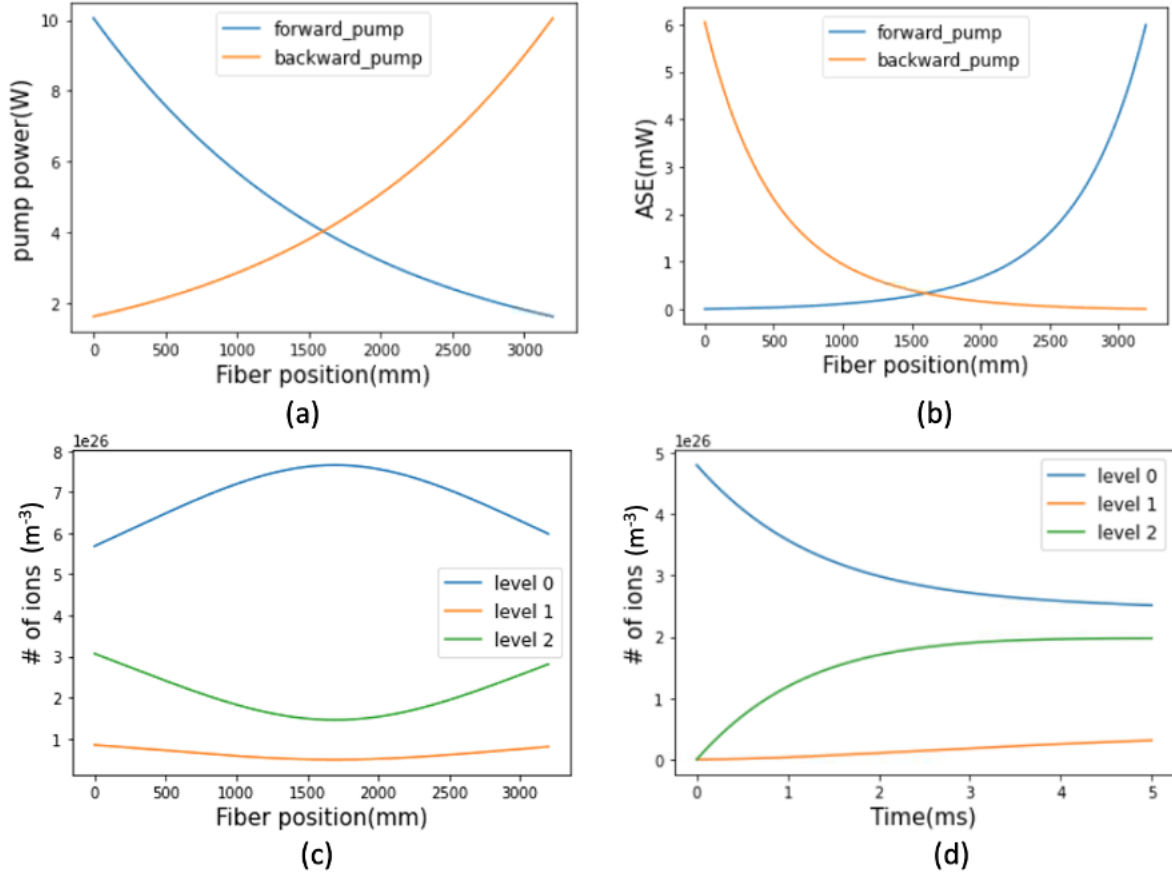
Figure 2. 10: At 20W pumping, simulated pump absorption(a), ASE(b) and (c) population density along 3.2m fiber amplifier; (d) time variation of the population density.

This model can be used to predict the stored energy. Stored energy is the total photon-flux energy that a fiber amplifier can generate, which mainly depends on pump power and ASE. Stored energy can be calculated as the formula:

$$E_{store} = h\upsilon A_{mode} \int_0^L \left(N_2(z) - N_1(z) \right) dz \qquad (2.21)$$

Where A_{mode} is the mode area. N_2 and N_1 are the Erbium ion concentrations in the upper and lower levels, which need to be integrated along the fiber. The predicted stored energies are shown in Fig. 2.11. For 30μm fiber, the stored energy is >350μJ at 30 W pump power. The more interesting results is in 50μm core fiber, where the stored energy can be up to ~mJ, indicating a potential goal for an experimental demonstration.
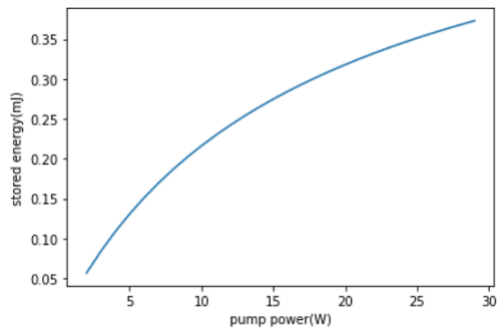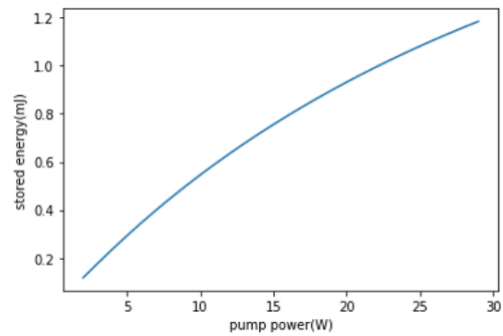
(a) (b)

Figure 2. 11: Predicted stored energies for (a) 30-µm-core-diameter and (b) 50-µm-core-diameter Er:ZBLAN fiber amplifiers.

Chapter 3 Large Core Er:ZBLAN Fiber Energy Exploration

3.1 Abstract

We explored the generation of high energy ns-short pulses in the mid-IR wavelength range using large core Er:ZBLAN fiber amplifiers. The highest energies achieved were ~0.7-mJ at 2.72-µm in 11.5-ns long pulses, with the corresponding peak power of 60.3 kW, obtained with a 70-µm diameter core fiber amplifier pumped at 976 nm and seeded by an KTiOAsO4-based optical parametric oscillator/ amplifier (OPO/OPA) system. These pulse energies are 3 times higher than previous high energy results using Mid-IR Fiber laser systems. These preliminary results enable us to pursue mJ-range pulse generation in large core Er:ZBLAN fiber amplifiers.

3.2 Introduction and motivation

Er:ZBLAN is a relatively new type of fiber material, and previous work using this material has largely focused on exploring high-power CW mid-IR lasing [75-77]. More recently, there has been increased interest in exploring pulse generation in the mid-IR using these fibers [78, 79]

37

due to their potential applications in spectroscopy, laser surgery, defense, gas monitoring, and IR-laser pumping (see chapter 1.2).

Q-switching was the dominant approach for exploring high-energy pulse generation with ~100-ns or longer pulse durations. For example, Frerichs et al. reported the first Q-switched 3-μm fiber laser using an acousto-optic modulator, obtaining 2.2-μJ, 100-ns pulses, corresponding to a peak power of 2.2 W [82]. Passive Q-switching and mode-locking have also been demonstrated with an average power of a few milliwatts by using InAs or gallium saturable absorbers [83, 84].

Since the publication of this early work, there has been a continuous improvement in output peak powers and pulse energies. In 2011, Tokita et al. reported 100-μJ and 90-ns pulses, corresponding to the peak power of 0.9 kW [85]. In 2017, generation of 150 μJ and ~100-ns pulses, corresponding to ~1.6-kW peak power, was reported by Yanlong et al [86], which is the highest pulse energy reported prior to the results produced by our research group. The motivation for this work is to achieve higher pulse energies and shorter pulse durations than previously published work using Er:ZBLAN fiber lasers and to understand the limits for high-energy storage and extraction. Also we seek to demonstrate the optical-damage limitations of high-energy extraction with ns-range pulse durations and compare to mature fused-silica glass fibers operating below 2.2 μm.

This chapter presents the methods used to generate high-energy pulses in large-core Er:ZBLAN fibers. An experimental test system was configured as a pulse-seeded fiber amplifier. Section 3.3 presents the seed source, a KTiOAsO4-based pulsed optical parametric oscillator/optical

parametric amplifier (OPO/OPA) system, which provides high seed-pulse energies for

Er:ZBLAN amplifier energy extraction testing. Section 3.4 discusses the high energy result by

Er:ZBLAN fiber amplifiers: 0.7-mJ energy in 10-ns long pulses are demonstrated from a 70-µm

core Er:ZBLAN fiber amplifier. Section 3.5 presents the nonlinear measurement and analysis in

fiber amplifiers. Section 3.6 discusses the limitations of the parametric amplifier system.

3.3 High energy nanosecond 2.75-µm parametric source

To explore the use of Er:ZBLAN fibers for high energy results, we used a 2.75-µm parametric

source developed by Prof. Jovanovic's research group [87] as the seed. A schematic of the

experimental setup of the KTA-based MOPA system is shown in Fig 3.1.
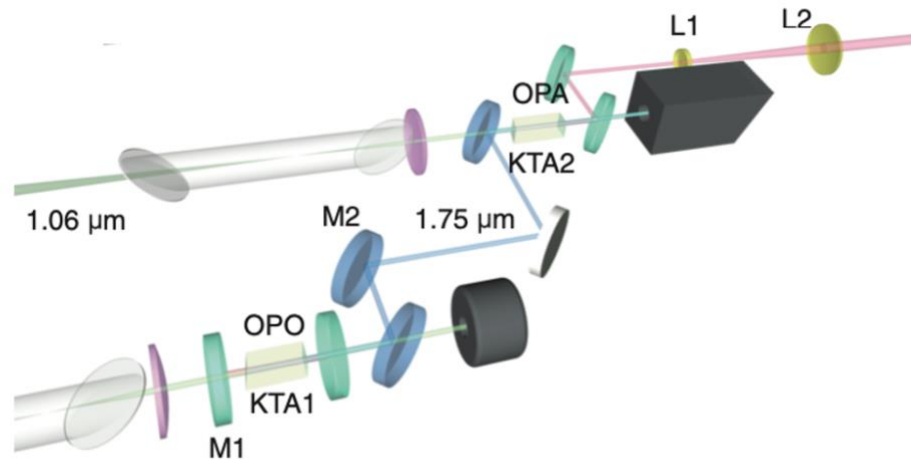
Figure 3. 1: Experimental setup of KTA-based MOPA system [87]

This KTiOAsO4-based MOPA is pumped by a Spectra-Physics Q-switched Nd:YAG laser

(Quanta-ray PRO-250-10H), which is seeded by a Lightwave injection seeder to provide single-

longitudinal-mode operation. The pump laser can deliver 1.064-μm, 10-ns, 10 Hz pulses with tunable energy of up to 1.4 J at a repetition rate of 10 Hz. The RMS energy stability and pulse-to-pulse timing jitter are 2.4% and 0.46 ns, respectively [88]. This MOPA system starts from the master oscillator (OPO), which employs a 5 mm×5 mm×20 mm KTA crystal (KTA1 in Fig 3.1) from Castech Inc. The crystal is XZ cut at θ ≈ 59∘ for type-II (eo-o) phase matching. Two coated mirrors (M1 in Fig 3.1) generated a simple parallel plane cavity with a length of ~24mm, which has high transmission at the pump wavelength at 1.064 μm and idler wavelength at ∼1.74 μm, and high reflection at a signal wavelength ~2.75µm. The pump beam is imaged by using a telescope from the laser to the OPO crystal, which also collimates and demagnifies the beam to minimize the angular dephasing and to increase the peak power for the parametric process. Since the laser focuses within the telescope, the light path is protected by the vacuum tube. The idler beam with a wavelength of 1.75µm is extracted after the OPO stage and is collinearly combined with the imaged, demagnified, and collimated 1064nm pump in a 5 mm×5 mm×25 mm KTA crystal (KTA2 in Fig. 3.1) with the same cut as KTA1 in the next OPA stage by using short-pass dichroic mirrors (M2 in Fig 3.1) with a 1.5µm cutoff wavelength. Then the signal beam is extracted by a dichroic mirror M1 to seed the Er:ZBLAN fiber amplifier in the next stage.

This parametric seed source (OPO/OPA) is wavelength tunable and thus allows maximization of the spectral overlap between the seed-pulse spectrum and the Er:ZBLAN amplifier gain spectrum. Since the OPO/OPA signal spectrum is narrower than the Er:ZBLAN fiber amplified spontaneous emission (ASE) spectrum, spectral matching was achieved by tuning the seed-pulse spectrum to approximately the center of the ASE spectrum, as shown in Fig. 3.2 (a). The measured temporal trace of 11.5-ns long seed pulses from this OPO/OPA system is shown in

40

Fig. 3.2 (b). Because the OPO/OPA output energy can be adjusted by changing the pump pulse energy from the Nd:YAG laser, this arrangement allows us to select any seed energy as needed from a range of spanning from a few-µJ up to 2-mJ shown in Fig.3.3. This was more than sufficient for Er:ZBLAN fiber amplifier seeding experiments, in which the highest seed energies used were below 200 µJ.
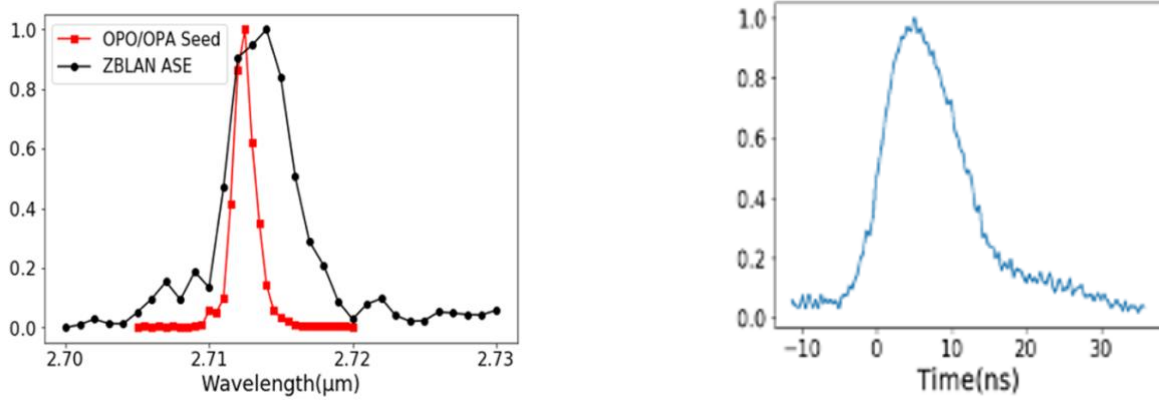
Figure 3. 2: (a) Measured spectra of OPA idler signal and Er:ZBLAN fiber ASE. (b) Measured signal pulse trace from OPO/OPA system.
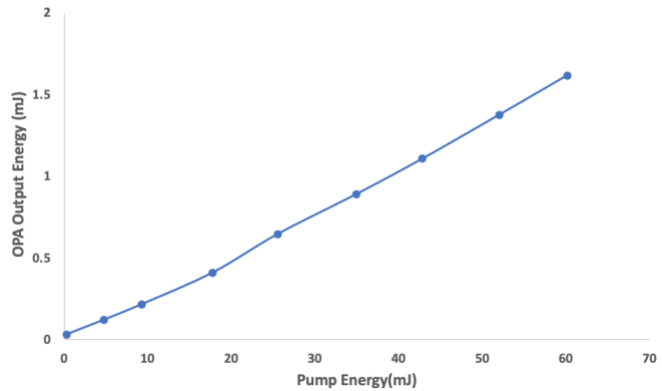
Figure 3. 3: KTA MOPA system output energy vs pump energy.

3.4 Large core Er:ZBLAN fiber amplifier experiment result

The fiber amplifier setup that was used for carrying out high-energy pulse experiments is built using a 0.8-m long piece of 70-µm core Er:ZBLAN double-clad fiber (Fiberlabs, Inc.) as shown in Figure 3.4. The fiber core is highly doped (6 mol. % Er3+ concentration) and has a numerical aperture (NA) of 0.12. Both fiber ends are polished at 12º to prevent ASE and amplified signal feedback into the core, suppressing lasing. The fiber inner-cladding diameter is 250-µm, which is surrounded by the 460-µm diameter polymer outer cladding, providing a pump-guiding NA of 0.55.

 This amplifier is pumped usinga 976-nm pump diode, which is coupled to a delivery fiber with a 400µm diameter core and NA of 0.22. The available pump power from this diode significantly exceeds the powers used in the reported experiments since heating of the 70-µm core Er:ZBLAN fiber limited the usable pump power. To mitigate heating, the 976nm pump beam exiting the delivery fiber was evenly split into two beams to pump the amplifier through both fiber ends. For thermal management, both ends of the Er:ZBLAN fiber amplifier were mounted onto water-cooled metal fixtures, and the protruding bare-fiber portions were additionally cooled using forced air flow. The 976-nm pump and 2.7-µm signal are coupled into and out of the Er:ZBLAN fiber using CaF2 lenses, which exhibit high transmission for both wavelengths. The lenses were uncoated, resulting in the total Fresnel losses of 5% and 8% per lens for signal and pump beam, respectively. Dichroic mirrors (with high reflectivity at 2.7 µm, and high transmission at 975 nm) designed for 45° incidence were used to separate signal and pump beams at the amplifier input and output.
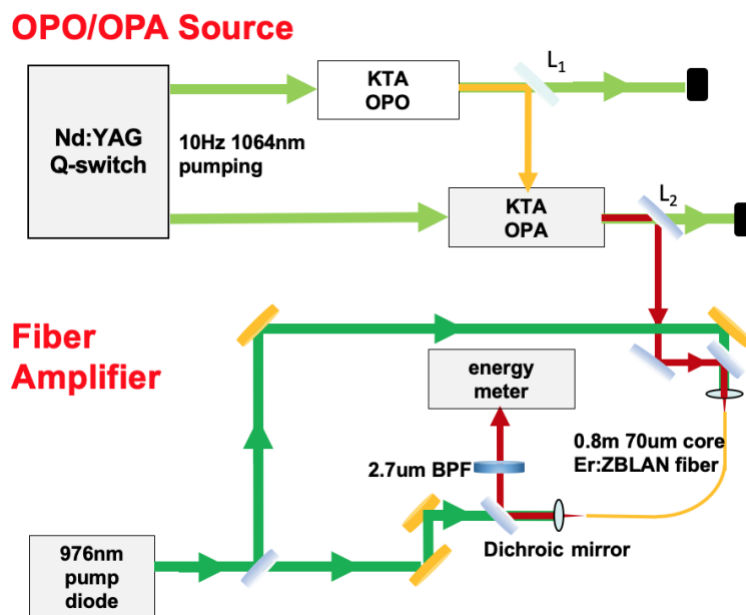
Figure 3. 4: Experimental setup of the 70-µm-core Er:ZBLAN fiber pulse amplification system

The measured amplified pulse energy from a 70-µm core Er:ZBLAN fiber as a function of the total coupled pump power (evenly split between both ends) for different seed-pulse energy is shown in Fig. 3.5. The pump power coupling efficiency in these measurements was 85%. All energy measurements in these experiments were done using a pyroelectric energy meter (Ophir PE10-C). The three lowest curves in the figure correspond to the amplification of seed pulse energies of 16.2 µJ, 39.5 µJ, and 81.3 µJ. For these measurements, we kept the seed pulse energy fixed while varying the pump power. Up to ~450 µJ of amplified pulse energy was produced at the highest pump power for the 81.3-µJ input. In order to explore the maximum extraction of the stored energy, we also characterized this amplifier with 142.5-µJ seed pulses (the upper curve in the Fig. 3.5). In this case, the highest output energy reached was 693 µJ at 12.9 W of coupled pump power. Since the measured pulse duration is 11.5 ns, the corresponding peak power at this highest energy is 60.3 kW. Comparing this "top" curve with the lower ones in Fig 3.5, one can

observe that it does not converge to zero at zero pump power, which is due to a significant fraction of the output consisting of the input-seed energy. This indicates that in this case the amplifier was operating under deep-saturation conditions.
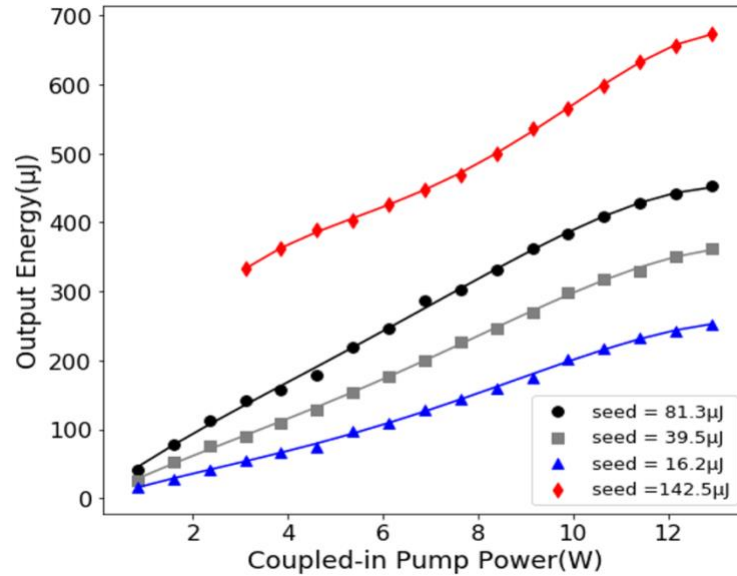
Figure 3. 5: Measured 70-μm-core fiber output energy for different input seed energy

For verification, we used the Frantz-Nodvik model [89] to estimate the amount of stored energy in this amplifier under various pumping levels. This can be done at each pump power level by comparing the small-signal gain, measured with a weak, seed signal that does not saturate the amplifier, to the high-energy pulse gain, measured with several different seed energies, each sufficiently high to cause partial amplifier saturation. This comparison allows the determination of the energy extraction efficiency for each seed-pulse energy [90], from which, using the measured output energy, one can calculate the stored energy in the fiber amplifier at this pumping level. The formula can be written as:

$$G_p = \frac{E_{out}}{E_{in}} \; \frac{ln\frac{G_0 - 1}{G_0^{1-\eta} - 1}}{ln\frac{G_0 - 1}{G_0^{1-\eta} - 1} - ln\frac{G_0}{G_0^{1-\eta}}} \tag{3.1}$$

Where G_0 is the small signal gain, G_p is the actual pulsed saturated gain, E_{out} and E_{in} are the output energy and input energy respectively, and η stands for energy extraction efficiency. First in the experiment, the small-signal gain G_0, measured at output energies well below saturation, is shown in Fig. 3.6 (black curve).
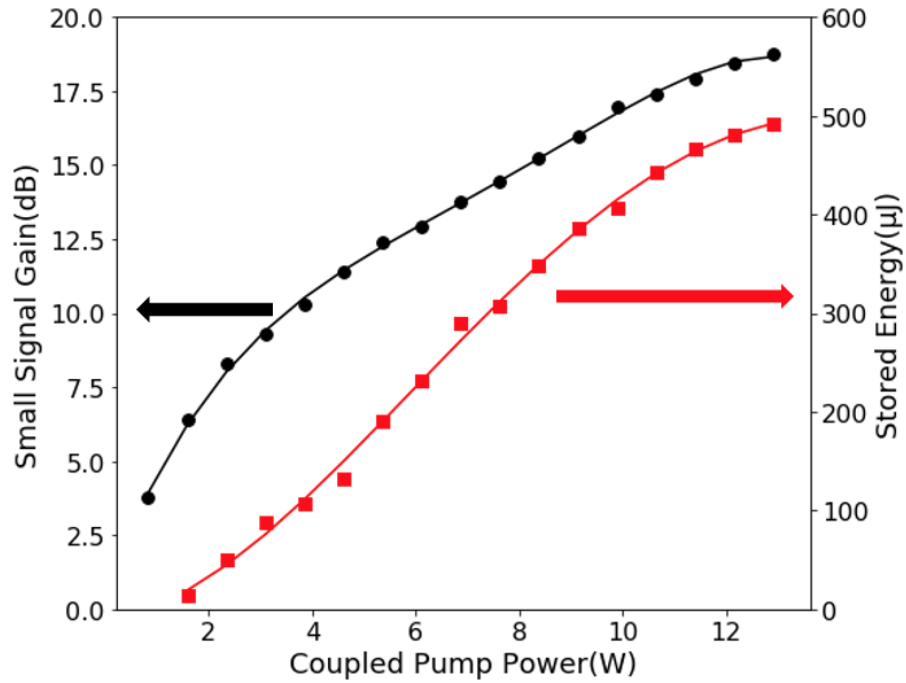
Figure 3. 6: Measured stored energy and small-signal gain of 70-μm-core Er:ZBLAN fiber

The relationship between η and G_p can be derived by equation (3.1). Fig. 3.7 shows two different curves with small signal gain with 12.9 dB and 18.7 dB respectively. The pulsed gain can be

calculated from measured output amplified energy, which is able to derive the extraction efficiency (x-axis in Fig. 3.7). Thus, the stored energy can be calculated using the formula: $E_{store} = \frac{E_{out}}{\eta}$. For instance, the measured stored energy 492µJ at $G_0 = 18.7$dB and 230µJ at $G_0 = 12.9$dB is marked in Fig. 3.7.
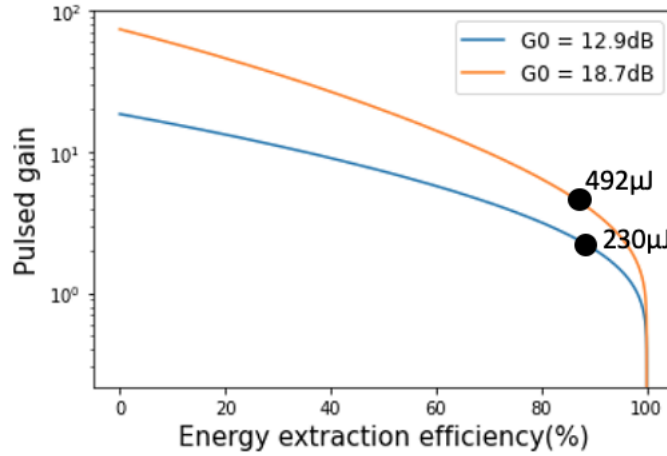
Figure 3. 7: Energy extraction efficiency vs saturated pulse gain

The estimated stored energy varying with pump power is also shown in Fig. 3.6 (red curve). One can see that this estimate indicates a near-complete extraction of the stored energy by the 142.5-µJ seed. Indeed, measured output energies for this seed are approximately equal to the sum of the input and the stored energy.

The achieved energy in the experiments with the 142.5-µJ seed were limited by a consistent optical damage at the output facet of the fiber shown in Fig. 3.8, occurring every time coupled pump power was increased above the level used for reaching ~690-µJ output pulse energy. Because this is the preliminary experiment, the fiber ends in our experiments were not protected by endcaps at that time, limiting the achievable pulse energy. We anticipate that this surface

damage will be eliminated once the protective endcaps are fused to the fiber ends in the future experiments (see chapter 4). Note also that there was a significant fiber heating at both ends of the fiber: the fiber tip temperature reached 110° C at 12.6 W of coupled pump power. We associate this with the high Er-doping concentration in the fiber, as well as with the fact that the pumping wavelength was exactly at the absorption peak, thus maximizing the heat load at each fiber end. Further mitigation of this heating should be achievable by partial detuning of the pump wavelength off this absorption peak.
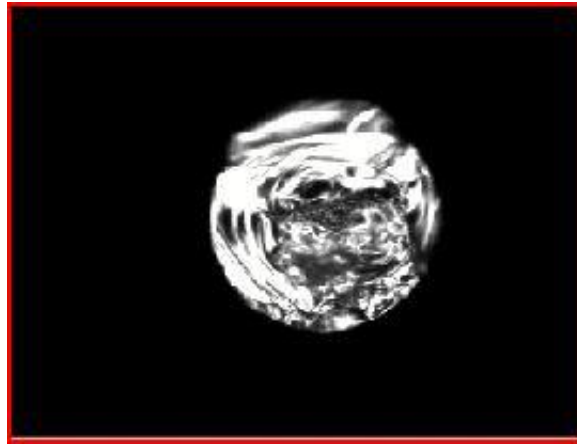
Figure 3. 8: damaged Er:ZBLAN fiber output facet

3.5 Nonlinearity in Er:ZBLAN fiber amplifiers

Self-phase modulation (SPM) gives rise to an intensity-dependent nonlinear phase shift, which is given by [91]:

$$\Phi_{NL} = \gamma P_0 L_{eff} \qquad (3.2)$$

where $\gamma = (n_2\omega_0)/(cA_{eff}(\omega_0))$ is the ZBLAN fiber nonlinear coefficient at the carrier frequency ω0, corresponding to the central wavelength at 2.8 µm, where n2 = 2.1×10^{-20} m²/W is the nonlinear refractive index of the ZBLAN fiber, c is the speed of light in vacuum, and $A_{eff}(\omega_0)$ is the effective mode field area of the fiber core. P_0 is the peak power of the fiber; L_{eff} is fiber effective length. For a signal at 2.8µm, a fiber with a 70 µm core diameter, $\gamma = 1.22 \times 10^{-5}$ W⁻¹/m, and the peak power is 60.3kW. So, the nonlinear phase caused by SPM is 0.255. From published data, the spectrum broadening is initially observed in 15.5µm core diameter single mode fiber amplifier at 52.7 µJ for ~5ns pulses [92]. In this condition. SPM induced nonlinear phase is 0.937, which is ~4 times than our large core fiber amplifier results. Thus, the SPM indued spectrum broadening can be ignored in our experiment. The Input seed and amplified signal are also measured in Fig. 3.9, and no spectral broadening was observed, indicating the energy we achieved is below the SPM threshold.
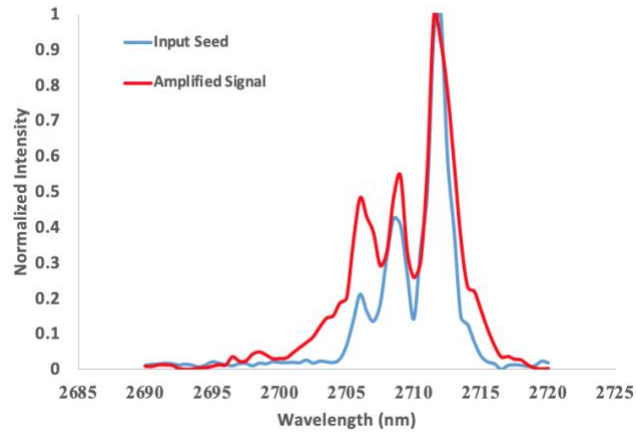
Figure 3. 9: measured input and output spectrum of 70µm-core Er:ZBLAN fiber amplifier at 690µJ pulse energy

Furthermore, the critical peak power for Raman threshold is given by:

$$\frac{g_R P_0^{cr} L_{eff}}{A_{eff}} \approx 16 \tag{3.3}$$

Where Raman-gain coefficient g_R for ZBLAN at 2.8 µm is 1.15×10^{-13} m/W. and calculated Raman threshold P_0^{cr} is 6.76×10^5 W. Thus, stimulated Raman scattering cannot occur at 60.3kW amplified peak power. From the published data on the stimulated Raman scattering in ZBLAN glass [93] the expected long-wavelength shift at 2.72 µm is ~430nm, corresponding to ~17-THz Raman frequency shift. The output spectrum measured in the 2–4 µm range at the highest output pulse energies is shown in the Fig. 3.10. It does not show any presence of stimulated Raman scattering, thus indicating the absence of nonlinear effects at the highest achieved pulse energies and peak powers. Also, according to [91] if the laser linewidth is exceeding 10MHz, Stimulated Brillouin Scattering (SBS) cannot be effectively excited. The input signal ~200Ghz linewidth indicated the SBS can be ignored.
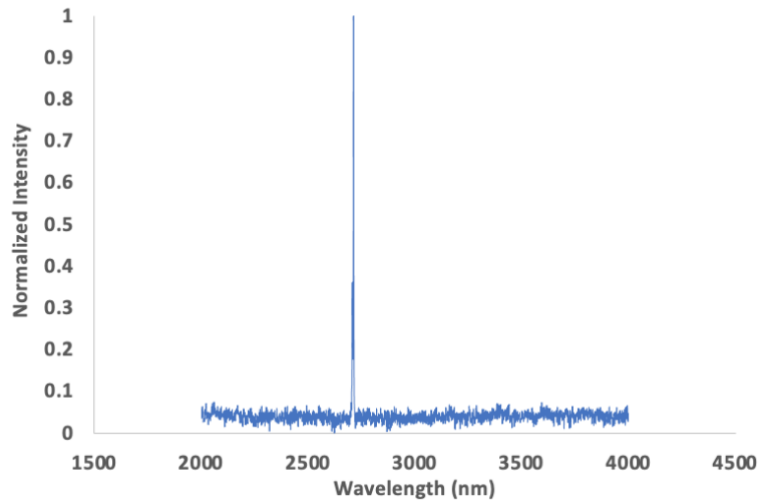
Figure 3. 10: measured output spectrum of 70µm-core Er:ZBLAN fiber amplifier in the 2–4-µm range at 690µJ pulse energy

3.6 Limitation of parametric source

We achieved 0.7mJ from a 70μm-core-diameter Er:ZBLAN fiber amplifier, but There are some limitations of parametric OPO/OPA sources. Figure 3.11 shows a near-field transverse beam profile of the 2.72μm idler from the OPO/OPA stage measured by the InSb camera (Xenics Tigris-640) [15]. The beam has a flat-top spatial profile which is shown in Figure 3.11 (a). The 2.1×1.8 mm signal shows a larger ellipticity of 1.15 and exhibits a stronger intensity lobe on the left side of the beam profile, which is in the walk-off direction. The beam quality analysis (M^2) for the OPO/OPA stage was performed using a CaF2 lens with a focal length of 100 mm. The formula for M^2 is given by:

$$W_x^2(z) = W_0^2[1 + \quad (\frac{M^2\lambda}{\pi W_0^2})^2(z - z_0)]$$

(3.3)

Where W_0 is the beam width at the waist, and z_0 is the waist position. For a single-mode diffraction limited beam, the M^2 value is 1. For an arbitrary beam, diffraction effects are stronger than for a single mode beam so the M^2 value will always be larger than 1. As shown in Figure 3.11(b), the beam quality factors of the 2.1 mm×1.9 mm signal beam from the KTA OPO/OPA stage were measured to be $M_x^2 = 2.0$ for the horizontal direction and $M_y^2 = 1.9$ for the vertical direction [87]. This type of non-gaussian laser beam is used for seeding the large core multi-mode ZBLAN fibers. The output beam of the Er:ZBLAN fiber amplifier is multi-mode without any doubts.

(a)   (b)
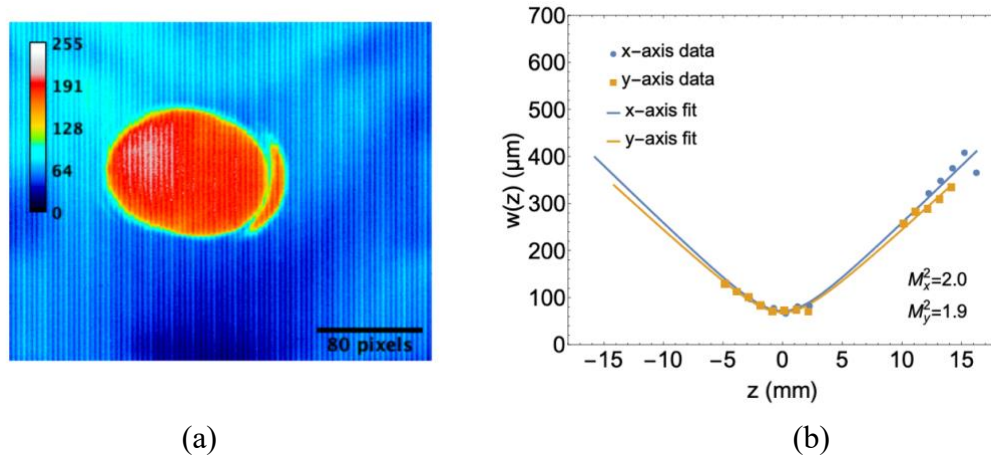
Figure 3. 11: time-integrated beam profile time-integrated beam quality(M^2) measurement for OPO/OPA stage [87]

Moreover, the commercial pumped laser is a Spectra-Physics Quanta-Ray flashlamp-pumped Q-switched Nd:YAG laser (PRO-250-10H). The laser operates at a fundamental wavelength of 1.064 μm at 10 Hz, which is used for pumping OPO/OPA systems. The generated idler (~1.74 µm) and signal(~2.75 µm) are also 10 Hz. This low reptation rate prevents the KTA based OPO/OPA system from achieving high average power. For Er:ZBLAN fiber amplifer system, while the system has a promising pulse energy, the laser average power is limited to 7mW.

Chapter 4 Single Mode High-energy Pulse Generation Using LMA Er:ZBLAN Fiber Amplifiers

4.1 Abstract

We explored and demonstrated single transverse mode, high energy, nanosecond short pulses in the mid-IR wavelength range using 30μm and 50μm large core Er:ZBLAN fiber amplifiers. The highest energies achieved are ~750 μJ at 2.78-μm in ~100ns long pulses, with a corresponding peak power of ~7.5 kW, obtained with a 50-μm diameter core fiber amplifier pumped at 976 nm and seeded by a ring-cavity single mode q-switched Er:ZBLAN fiber lasers. To the best of our knowledge, these results are the first and highest pulse energies and peak powers in single transverse mode achieved from large core Er:ZBLAN fiber lasers at wavelengths longer than 2.5μm with nanosecond pulses.

4.2 Background and Introduction

Recently, there have been numerous experimental studies exploring generation of high energy (100μJ to ~1mJ range) pulses and powers in mid-IR at ~2.8 µm using large core Er:ZBLAN

fiber lasers and amplifiers, with core sizes ranging from 30µm to 115µm [94, 95]. However, since these fiber cores are multimode, all the achieved high energies were produced in multimode output beams. For many applications it is preferable to maintain diffraction-limited output beam quality. In this Chapter, we demonstrate two methods that it is possible to achieve robust single mode high energy pulses from large core Er:ZBLAN fibers, which surpass the limitation of the single mode fiber pulse energy generations [115]. In section 4.3, the single mode source will be designed and developed as the seed for LMA fiber amplifiers. In section 4.4, the single mode excitation is introduced. This technique can produce a single mode output laser beam using multimode fibers. In section 4.5, we experimentally demonstrate high energy pulses in a single transverse mode from 50µm and 30µm core Er:ZBLAN fibers in mid-IR at ~2.8µm. In section 4.6, high-order mode filtering techniques will be introduced, which are more robust than single mode excitation techniques.

4.3 Single mode q-switch laser development

To replace the low rep-rate non-gaussian KTA OPO/OPA surrogate source, we designed and developed a single mode q-switched fiber laser source. The schematic setup is shown in Fig.4.1. Unlike with conventional linear cavity q-switched lasers [85, 96], we built the ring-cavity q-switched fiber lasers. This cavity can generate linear polarized light, which can propagate through an isolator and into the amplifier with low loss. In the setup, 4m, 18µm-core-diameter double-cladding Er:ZBLAN (FiberLabs Inc.) fiber was used as an active gain medium. The doping concentration is 6 mol.%. The fiber was spliced with 450µm-long AlF_3 as endcaps to protect the ends from the pulsed damage and degradation. Both ends are polished at an angle of

12º to avoid parasitic lasing. The inner cladding diameter is 250µm and NA is >0.5. The outer polymer cladding is 450µm in diameter. The pump absorption in the inner cladding at 976nm was measured as ~3dB/m. The fiber ends were hold by the water-cooling chuck holders with V-shaped grooves. Two 20mm plano-convex CaF$_2$ lens were used to form the cavity to focus the beam into the fiber and collimate the beam in free space. An isolator with 30-dB isolation (Faraday Photonics LLC.) is used in the cavity to block the converse ASE. An Acousto-optic modulator (AOM) made by germanium (ISOMET Corporation.) was inserted in the cavity as a q-switch, which is driven by a pulsed RF source at 120MHz. We used the first order mode of AOM for q-switching since the diffraction efficiency of AOM is only 70%. Q-switching with zero order will be limited by the diffraction efficiency for high energy operations. The half-wave-plate before the AOM is for controlling the polarization of beam through the AOM to maximize the diffraction efficiency.
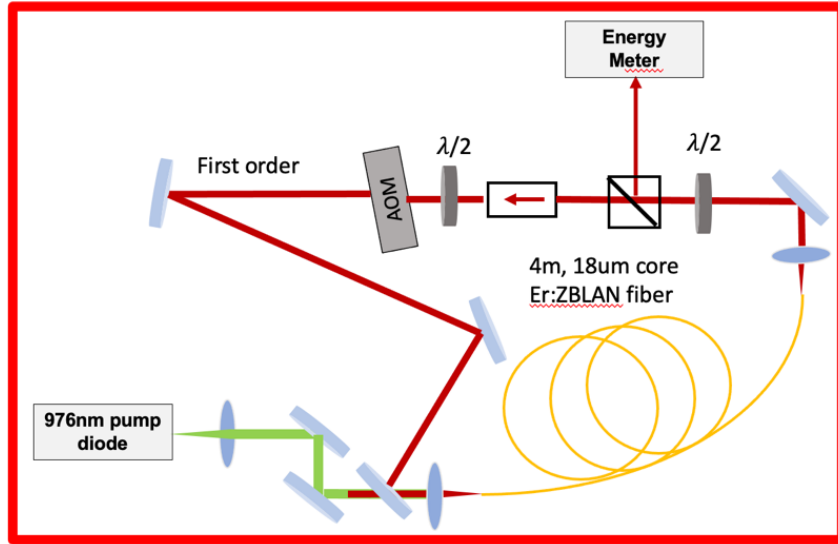
(a)
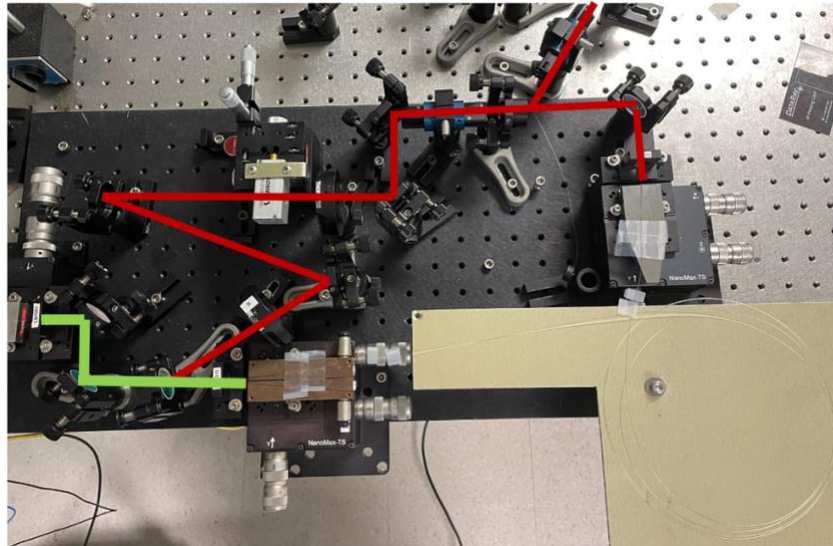
(b)

Figure 4. 1: (a) Schematic of ring cavity q-switched Er:ZBLAN fiber laser. (b) photo of ring cavity q-switched Er:ZBLAN fiber laser. The fiber is 4m 18μm-core-diameter Er:ZBLAN and polished at two ends.

The rep-rate of q-switch can vary from 100Hz to 5KHz. A pulse train at 1kHz is shown as Fig. 4.2 (a). The pulse duration is ~96ns as shown in Fig. 4.2 (b). The output energy as a function of

the pump power is shown in Fig. 4.3. It is clear to see the maximum energy is limited by 45µJ at

2-3W. The output energy is still increasing as pump power increased, but the output energy is

kept constant. We believe it is feedback from the laser system which depletes the ion population

in the upper level in this three level system, which generates CW lasing when the pump power is

larger than 2W. However, this energy is still enough to seed the subsequent fiber amplifier stage,

as typically we usually use less than 20µJ to seed the pre-amplifier.

Figure 4. 2: Screen shot of (a) 1kHz pulse train (b) pulse duration
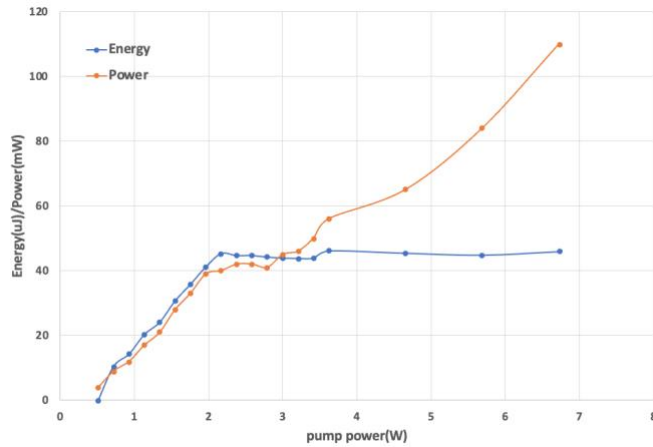
Figure 4. 3: Measured 18-µm-core q-switched laser output energy and output power at different

pump powers.

4.4 Single mode excitation technique with LMA fibers

Fibers with a large multimode core can produce a fundamental-mode output when used in combination with single-mode excitation technique in a multimode core. The single-mode excitation technique reported in [97] is illustrated in Fig. 4.4. The basic idea of this technique is to use the mode-matched beam coupled into a single-mode fiber to quantify the beam quality of the LMA fiber output. A gaussian beam is coupled into an LMA fiber, and the output laser beam of the LMA fiber is coupled into a single-mode fiber with a pair of lenses to control the mode field diameter, which acts as a spatial filter that only transmits the LP_{01} (fundamental) mode and filter the high order mode. The objective of this setup is to maximize the percentage of light with fundamental mode. The measured power transmission through the single-mode fiber provides a quantitative measurement of this percentage, and therefore of the mode quality at the LMA fiber output. In a first step of experiment, the fundamental mode field diameter (MFD) of the two fibers is calculated and measured. The two lenses between the two fibers are then selected for perfect mode matching. The telescope can be inserted between the stages to adjust the MFD. Finally, the launching conditions of the beam into the LMA fiber are adjusted to maximize the transmission through the single-mode fiber. This system also requires very precise positioning of the input beam, which should be strictly co-linear with the core axis, and very accurately positioned in the two directions transverse to this axis [98].
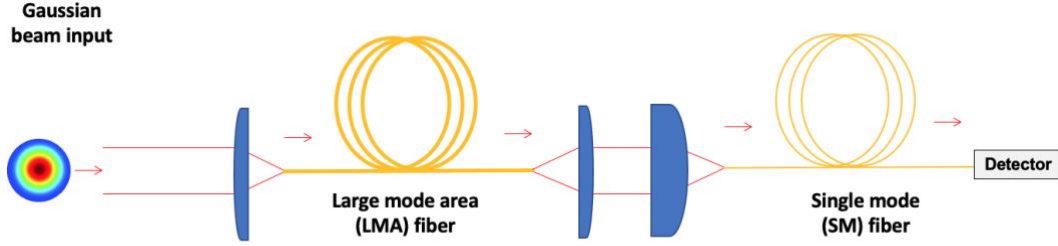
Figure 4. 4: Experimental setup to excite the fundamental mode in an LMA fiber

Moreover, the fundamental mode needs to be preserved while propagating along the fiber. The structural properties and packaging of an LMA fiber influence whether the fundamental mode will propagate undisturbed and reach the output without significant scattering into higher order modes. Mode scattering in LMA fibers is caused by intrinsic random refractive-index variations along the length of the fiber, characterized by a power spectrum S. Coupling occurs between two modes when the Fourier component $S(\Lambda)$ at the spatial frequency $2\pi/\Lambda$ corresponding to the beat length Λ between the two modes is sufficiently strong. The strength of the single mode to higher order mode coupling coefficient η increases with increasing magnitude of $S(\Lambda)$, the formular is given by [99]:

$$\eta = \frac{n^2}{2\pi^2} S(\Lambda) \tag{4.1}$$

Where n is the refractive index of the fiber and $S(\Lambda)$ depends on stress-induced index perturbations as well as micro-bends associated with the limited mechanical stiffness of a fiber structure [6], both of which developed during fiber fabrication. Fibers manufactured using rod-in-tube approach can exhibit significantly stronger scattering than fibers manufactured using modified chemical vapor deposition. For index guiding LMA fibers [100],

$$S(\Lambda) = \frac{\Lambda^4}{D_{out}^6} \tag{4.2}$$

where D_{out} is the fiber outer diameter, the strong dependence on diameter reflects the strong influence of fiber stiffness on the formation of micro-bends. This formula indicates that even a moderate increase in fiber diameter D_{out} can significantly reduce scattering. It also shows that mode scattering increases with increasing beat length between modes. According to this approximation [101], beat length between the fundamental and the closest higher order mode (typically the LP11 mode) in a step-index fiber is given by:

$$\Lambda = \frac{2.2nD_{in}^2}{\lambda}$$

(4.3)

Where D_{in} is the fiber outer diameter and λ is the excited wavelength. Combined equations (4.1) - (4.3). We can easily find the mode coupling efficiency η is given by:

$$\eta = 1.19\frac{n^6 D_{in}^8}{D_{out}^6 \lambda^4}$$

(4.4)

In the formula (4.4), mode coupling efficiency η proportional to n^6 and D_{in}^8 and inversely proportional to λ^4. Thanks for the effort in the near-IR wavelength range, the largest core sizes that could sustain such single-mode excitation were demonstrated to be in the 65µm - 80µm range [102]. It indicates that η should be lower in mid-IR wavelength range for same fiber geometry, which implies such single mode excitation should work for large core (<50µm) ZBLAN fibers operating at longer wavelength like 2.8µm.

4.5 Single mode high energy pulse amplification

LMA fiber amplifier experimental setup is shown in Fig. 4.5. The setup consists of four parts: Q-switched laser seed source, single mode fiber pre-amplifier, large core fiber amplifier and single mode fiber filter setup for aligning amplification stage excitation in a single transverse mode. Q-

switched laser source uses 4m single-mode doubled-cladding highly doped Er:ZBLAN fiber (6 mol. % Er^{3+} concentration), which is presented in section 4.3. The repetition rate can be tuned from 100Hz to 5kHZ. These seed pulses are coupled into the single mode 18µm-core-diameter fiber pre-amplifier using 25mm CaF2 lenses, the output energy of signal at 1kHZ is shown in Fig.4.6 (a). And the output signal wavelength is shown as Fig. 4.6 (b).
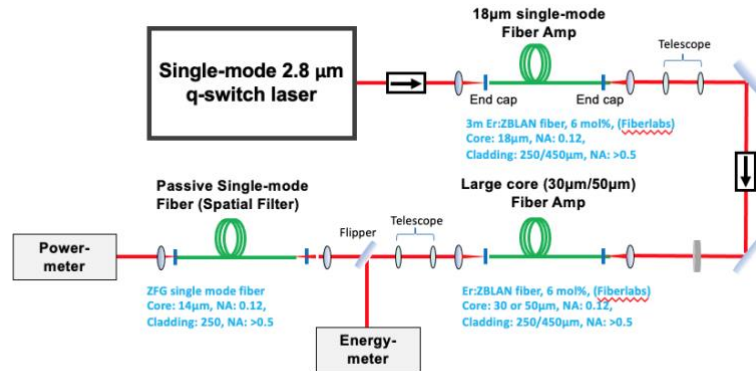
Figure 4. 5: Experimental setup of the Er:ZBLAN LMA fiber pulse amplification system;

(a)   (b)
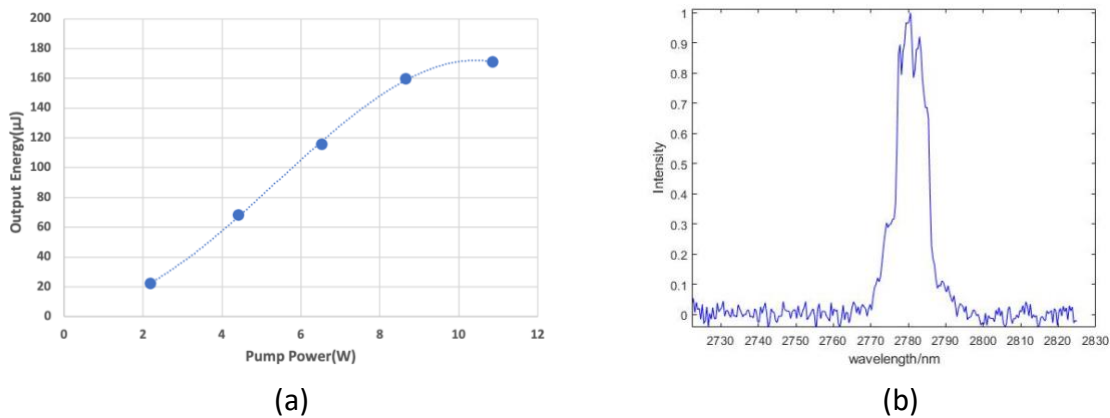
Figure 4. 6: (a) Energy and (b) wavelength from the single mode 18-µm-core Er:ZBLAN pre-amplifier

This pre-amplified seed can vary from 0 to ~180μJ, which is sufficient for seeding the subsequential LMA fiber amplifier. The amplified signal is coupled in to LMA fiber amplifier using CaF$_2$ lenses, and a 40mm focal length lens is chosen to match amplifier fiber fundamental mode. The LMA fiber amplifier uses highly doped (6 mol.% Er^{3+} concentration) Er:ZBLAN fiber (Fiberlabs, Inc), with a 50 μm diameter and 0.12 NA core. The fiber inner cladding diameter is 250 μm with >0.5 NA, and the outer cladding diameter is 460 μm. Both fiber ends are protected with AlF$_3$ as endcap to protect ZBLAN from damage and degradation. The angle of the endcaps is polished as 12° to prevent lasing. We used a fiber coupled pump diode providing up to 75 W at 976 nm from a 400 μm and 0.22 NA delivery fiber, which was coupled into the Er:ZBLAN fiber from two ends. And the output energies were measured using a pyroelectric energy meter (PE 10-C P/N 7Z02932) which is shown in Fig. 4.7(a). The seed is kept at 30μJ from 500Hz to 5kHz. The achieved output energies varied from 349μJ at 5kHz to 743μJ at 500Hz. We noticed the energy at 500Hz and that at 1kHz has the similar pattern. It indicates that the gain recovery time of this 3.2m 50 μm core fiber at 21 W is around 1ms-2ms same as the model prediction (chapter 2.6). And after single mode excitation, the measured beam quality of the 50μm core and 3.2m long fiber output after this procedure is shown in Figure 4.7 (b), indicating M^2 ~1.245.
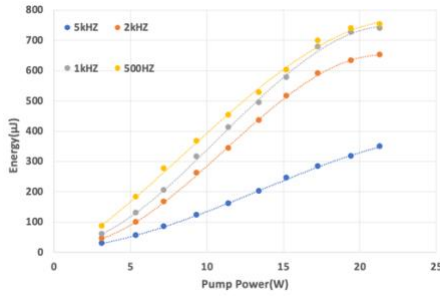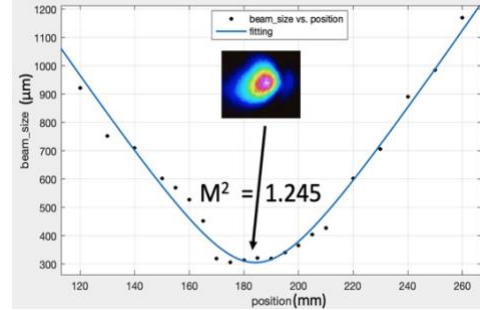
(a)   (b)

Figure 4. 7: (a) Output energy from 50µm core Er:ZBLAN fiber amplifier using 30µJ seed in different rep-rate; (b) Mode quality of output beam from 50µm core Er:ZBLAN fiber amplifier

To verify the stored energy, we used the Frantz-Nodvik model (chapter 3.4) to experimentally estimate the amount of stored energy in this amplifier, under various pumping levels. The small signal gain and measured stored energy is shown in Figure 4.8. One can see that ~80% of stored energy is extracted with the 30µJ seed.
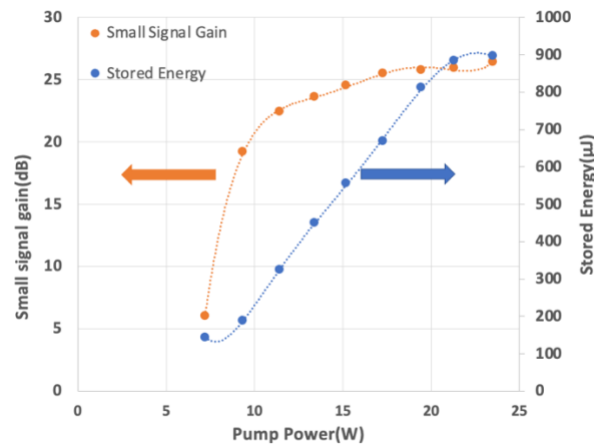
Figure 4. 8: Small signal gain and stored energy of 50µm core Er:ZBLAN fiber amplifier

However, perfect matching of the simulated data (chapter 2.6) with the experimental data could not be achieved. The discrepancies come from two aspects (the error of the experiments). One is

because the ZBLAN is soft glass material, and deforms especially at high power. It will affect the coupling efficiency, thereby, affect the measurement accuracy. The other is the pump loss. Pump leakage can reduce the population inversion in the laser system, and thus reduce the stored energy.

We also performed an additional set of high-energy amplification experiments, in which the 50-μm core fiber was replaced with a smaller-core fiber. Specifically, we used 1.9 m of highly doped (6 mol. % Er^{3+} concentration) Er:ZBLAN double cladding fiber (Fiberlabs, Inc), with the 30-μm diameter and 0.12-NA LMA core. The fiber inner cladding diameter was 300μm with >0.5 NA, and the outer cladding diameter was 460μm. The measured amplified pulse energies for 97.3-μJ seed for 5kHZ rep-rate is shown in Fig. 4.9 (a). The highest obtained pulse energy in these experiments were up to 419μJ. In this 30-μm core fiber, the maximum achieved pulse energy was limited by fiber end heating. The measured $M^2 = 1.289$ is shown in Fig. 4.9 (b).
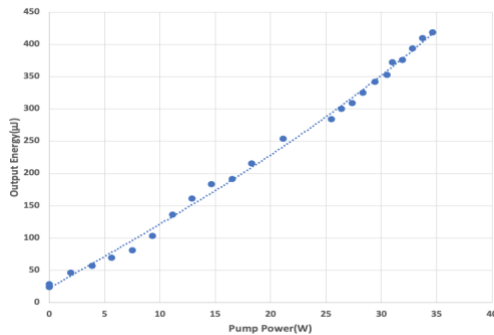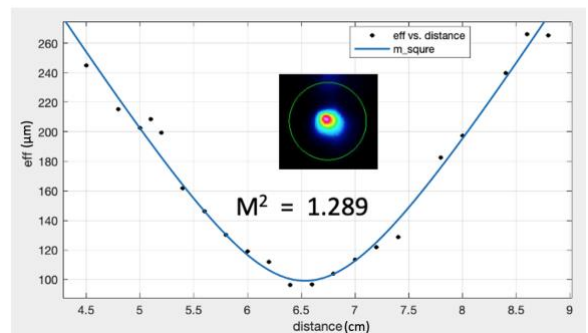
(a)   (b)

Figure 4. 9: Output energy from 30μm core Er:ZBLAN fiber amplifier; (b) Mode quality of output beam from 30μm core Er:ZBLAN fiber amplifier

4.6 High-order mode filtering in a coiled ZBLAN fibers

The other common way a large-mode-area (LMA) fiber h can produce a fundamental-mode output is high-order mode filtering in a coiled fiber. This coiled-LMA technique is first reported by Koplow in 2000 [103]. Compared with single mode excitation techniques, it is relative insensitivity to external perturbations, and thus became the basis for the majority of current commercial LMA fiber laser systems. Coiling-induced loss in an index-guiding fiber is caused by frustrated TIR at the curved core-cladding interface [104]. Mode differentiation becomes possible since the mode field penetration into the cladding increases with increasing mode order. The bend loss formula for different mode order is given by [105]:

$$2\alpha = \frac{\pi^{1/2}\kappa^2 \exp\left(-\frac{2\gamma^3 R_{\text{eff}}}{3\beta_z^2}\right)}{2R_{\text{eff}}^{1/2}\gamma^{3/2}V^2 K_{m-1}(\gamma a)K_{m+1}(\gamma a)} \tag{4.5}$$

Where the 2α represesntes power loss coefficient; κ is field decay rates in core; γ is field decay rates in cladding and K_m is modified Bessel functions. The main objective is to choose the critical bending radius R_{ij} (at which the LP_{ij} mode starts radiating into the cladding) such that it is larger for all higher order modes than for the fundamental mode. The coil radius such that $R_{01} < R_{coil} < R_{11}$ allows suppressing all higher order modes while preserving the fundamental mode. We simulated a 30µm core diameter Er:ZBLAN fiber for bending loss for different mode orders. The bending radius $R_{coil} = 2.3$ cm for 10dB/m LP_{11} loss if we use commercial ZBLAN fibers with 0.12 NA. This coiling radius is even tighter than the break radius of ZBLAN. Thus, we try to customize design the 30µm-core-diamdter with 0.1 NA, therefore $\Delta R = R_{11} - R_{10}$ is larger. The

bending radius R_{coil} can go up to ~5cm, which is more convenient to packing this type of fragile

ZBLAN fibers.
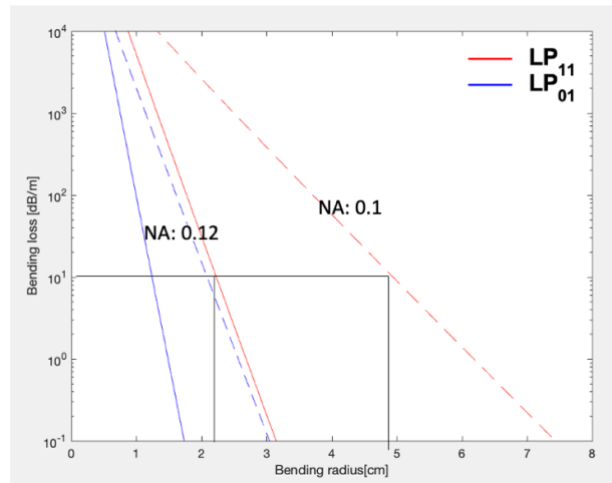
Figure 4. 10: LP_{11} and LP_{01} modes calculated loss versus bend radius for a coiled 30μm core diameter LMA ZBLAN with different NA.

Chapter 5 Mid-IR Fiber CPA Design

5.1 Introduction and background

Up till now, Er:ZBLAN fiber amplifiers for nanosecond range pulse have been thoroughly

explained and demonstrated in chapter 2 - 4. However, there is a lack of research for high energy

ultrashort pulses generation in Mid-IR range. Er:ZBLAN based Fiber CPA is an efficient way to

generate high energy femtoseconds pulses. In this Chapter, we will introduce the design of first

Mid-IR FCPA system. Our designed setup is shown in Fig. 5.1, which includes mode locking

seed and nonlinear amplifier to generate broadband high-energy pulses, stretcher to stretch the

ultra-short pulse to ~ns range, multiple amplifier stages to amplify nanoseconds pulses to ~mJ

range, and compressor to compress pulses into femtoseconds range. In this chapter, 5.2 will

introduce the details of mode locking laser and nonlinear amplifiers. 5.3 will introduce the initial

design of stretcher and compressor.
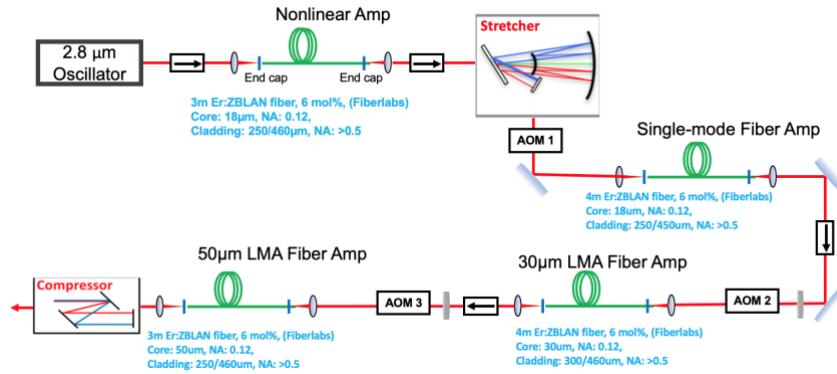
Figure 5. 1: Schematic of Er:ZBLAN based FCPA

5.2 Mode locking and nonlinear amplifier

The mode locking oscillator is important for the FCPA system to generate single mode femtosecond seed pulses. The nonlinear polarization rotation (NPR) mode locking oscillator we built is shown in Fig. 6.2. We used 2.5m heavily doped Er^{3+} concentration ZBLAN fibers (LeVerre Fluoré) with 15 µm core (NA = 0.12) and 240 * 260 µm double D-shaped inner cladding with NA >0.5. A quarter wave plate, a free space optical isolator and a half wave plate as an artificial saturable absorber are inserted into the ring cavity.

(a)

(b)
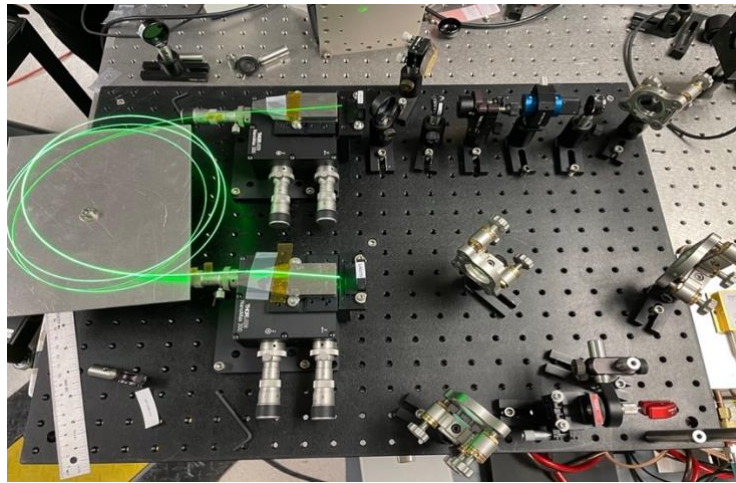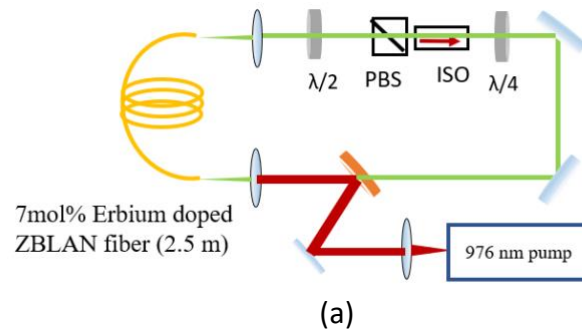
Figure 5. 2: (a) Schematic and (b) Experimental setup of Er:ZBLAN mode-locking system;

The oscillator produces, 3.35nJ, 222mW average power with 66.14MHz pulse train. The optical

spectrum at 2786nm with bandwidth 22 nm is shown as Fig 5.3 (a). Since the ZBLAN fiber has

the anomalous dispersion at ~2.8 µm, the mode-locking pulse has a soliton shape. The

autocorrelation trace measurement is shown in Fig 5.3 (b), which indicate the pulse duration is

~380 fs.

(a)   (b)
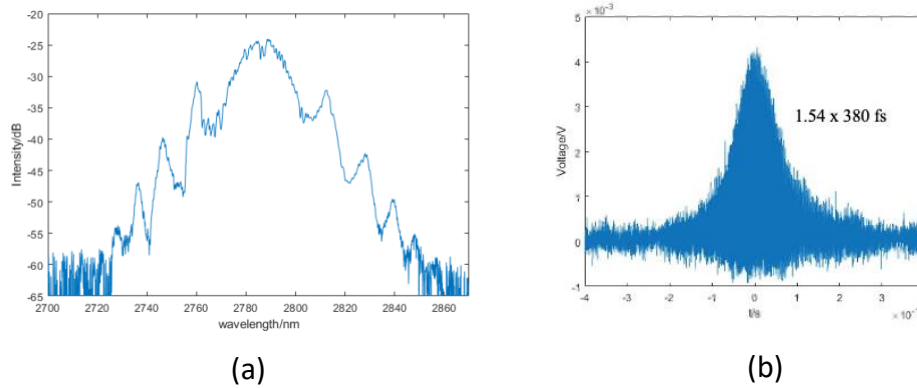
Figure 5. 3: Measured (a) Output spectrum (b) autocorrelation trace of the oscillator.

Due to the low energy (~3nJ) and narrow spectrum bandwidth (~20nm) of the oscillator, we decided to add a nonlinear amplifier before the stretcher to amplify the signal as well as broaden the spectrum. According to the simulation, using 2.5m Er^{3+}: ZBLAN fiber amplifier at 4W pump power, the output pulses duration 91fs and bandwidth ~100nm is shown in Figure 5.4. The pulse energy can go up to 25nJ.

(a)   (b)
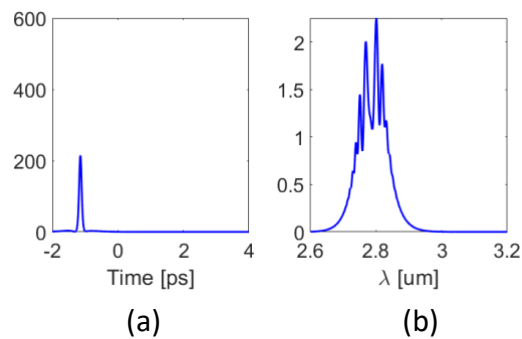
Figure 5. 4: Simulated Output (a) duration (b) spectrum of the nonlinear amplifier.

5.3 Stretcher and compressor design

The stretcher and compressor are the most important parts for the FCPA system. An aberration-free stretcher based on Offner-triplet is designed to provide pulse stretching. The schematic of the stretcher is shown in Fig. 5.5.
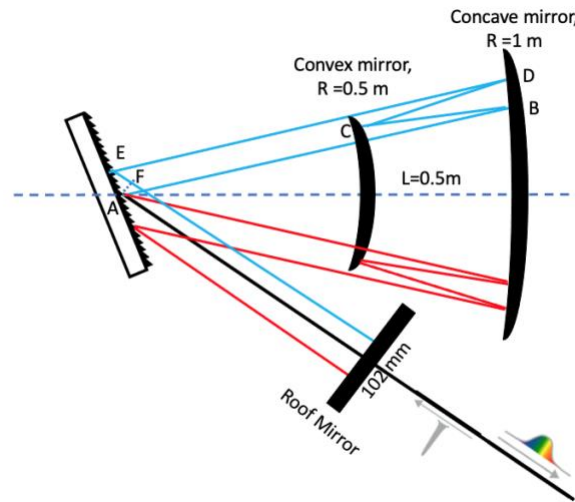
Figure 5. 5: Schematic of designed Offner stretcher.

The combination is composed of two spherical concentric mirrors. The first mirror is concave while the second one is convex. This combination presents interesting properties for use in a pulse stretcher. It is characterized by complete symmetry, so only the symmetrical aberrations can appear, i.e., spherical aberration and astigmatism. But the presence of two spherical mirrors whose radii of curvature ratio is 2 and of opposite sign cancels these aberrations [106]. This combination has no on-axis coma and exhibits no chromatic aberration because all optical elements are mirrors [107]. The grating for stretcher we plan to use is 600 grooves/mm with 120 × 140 mm dimension from Spectrogon Inc. The substrate material is Zerodur with 20mm

thickness. From the table 5.1 [108], the thermal expansion coefficient of Zerodur is negligible compared with another materials, which means the FCPA system can handle tens of watts. The curvature radius of concave mirror 1m and the distance between mirrors is 0.5m. The input light angle is 60.3º which is close to the Littrow angle 58.76º at 2.8μm. The reflection efficiency for Littrow angle at 2.8μm is ~95%.

Material	α (ppm/K)
Polycarbonate[16]	70
Aluminum[16]	22.7
Bronze[16]	≈ 17
Steel[16]	10–17
Optical Glass N-BK7[17]	7.1
Optical Glass N-ZK7[17]	4.5
Borosilicate Glass Duran®/Pyrex®[18]	3.3
Borosilicate glass E-6[19]	2.9
Silicon carbide Boostec® SIC[20]	2.2
Fused silica[21]	0.51
Titanium-doped fused silica ULE®[22]	0 ± 0.030
ZERODUR	0 ± 0.007

Table 5. 1: Thermal expansion coefficient of different materials

The phase function of this Offner stretcher is given by [106]:

$$\Phi_s = \frac{\omega}{c}P_s - \frac{2\pi}{d}AE \tag{5.1}$$

Where $P_s = AB + BC + CD + DE + EF$ (in Fig. 5.5) is the optical path length (OPL) and second terms is responsible for phase corrections. Fig. 5.6 shows the time delay for the different

wavelength. This Offner stretcher can stretch the ~100nm pulses (2750nm to 2850nm from

nonlinear amplimer) to ~1ns.
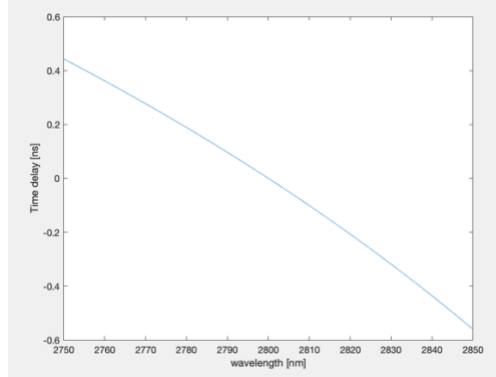
Figure 5. 6: Time delay verses wavelength range from 2750nm to 2850nm.

In this FCPA systems, the phase accumulated due to dispersions from materials or dispersive

optical components can be expanded as Taylor series:

$$\Phi(\omega) = \Phi_0 + \Phi_1(\omega - \omega_0) + \frac{\Phi_2}{2!}(\omega - \omega_0)^2 + \frac{\Phi_3}{3!}(\omega - \omega_0)^3 + \cdots \quad (5.2)$$

Where $\Phi_m = \left(\frac{\delta^m \Phi(\omega)}{\delta \omega^m}\right)_{\omega=\omega_0}$. The stretched pulse amplified by the Er:ZBALN fiber amplifier

need to compressed by the compressor. For several hundred femtoseconds pulses, the

compressor shown in Fig 5.7 is necessary to compensate the accumulated group velocity

dispersion (GVD) Φ_2 and third order dispersion (TOD) Φ_3 generated by stretcher and amplifiers

[71]. According to the dispersion parameters in ZBLAN fibers [108], calculated Φ_2 and Φ_3 for

the designed stretcher and 10m Er:ZBLAN amplifier is shown in table 5.2. the dispersion

accumulated by fiber is negligible compared with the designed Offner stretcher. Thus, the total

dispersions (last column in table 5.2) are close enough to that of stretcher. The compressor

design is shown in Fig. 5.7. In experiment, compressor can compensate the total GVD and TOD by adjusting he separation of gratings and the angles of incident beam.

	Stretcher	10m Fiber	Total
GVD (Φ_2)	70.1 ps^2	-0.86 ps^2	69.24 ps^2
TOD (Φ_3)	-1.56 ps^3	-4.4×10^{-2}ps^2	-1.6 ps^2

Table 5. 2: Second and third order dispersion for FCPA systems.
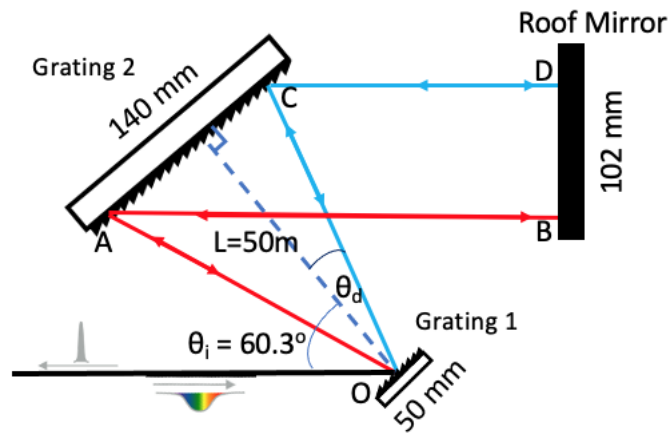
Figure 5. 7: Schematic of designed Compressor.

Chapter 6 Machine Learning Optimizer Algorithm for Coherent Pulse Stacking

6.1 Abstract

We apply momentum stochastic parallel gradient descent (MSPGD) and policy gradient in the context of algorithms to optimize coherent pulse stacking (CPS), and demonstrate their increased effectiveness compared to traditionally used stochastic parallel gradient descent (SPGD) algorithm.

6.2 Introduction and background

The high-power, high-energy Er:ZBLAN fiber amplifier system including Fiber Chirped-Pulse Amplification (FCPA) has been introduced and demonstrated in chapter 5. However, FCPA focuses on amplifying a single stretched pulse and hence its performance is limited by the nonlinearity and optical damage threshold in an optical gain medium. One way to circumvent this limitation and reach higher output peak power is to amplify multiple stretched pulses and coherently combine them in the time domain, producing a single pulse

at the output. In this chapter, we report several machine learning algorithms and optimizers which can be applied into combining systems. Also, we demonstrate the superiority of the machine learning algorithms including MSPGD and Reinforcement learning in the simulation of Coherent Pulse Stacking (CPS) system to optimize the phases of a 9 equal-amplitude pulse burst being stacked into a single output pulse.

6.3 Coherent Pulse Stacking (CPS)

Coherent Pulse Stacking (CPS) is a temporal combining technique, which can stack a burst of pulses coherently into one pulse using a series of Gires-Tournois interferometers (GTI) cavities [110, 111]. This technique extends the energy scaling capabilities of chirped pulse amplification (CPA) by ~two orders of magnitude, thus reducing fiber array size by a similar factor. However, analytically finding proper phases for pulse train is difficult due to complexity of a CPS system. To be more specific, CPS uses several cavities composed of mirrors and beam splitters, making it difficult to find the desired phases of a pulse train that would result in a stacked pulse with maximum peak intensity. Therefore, a good optimizer is required to efficiently find the correct phases and achieve maximum stacking efficiency. Moreover, Coherent Pulse Stacking (CPS) is mathematically equivalent to deep recurrent neural network [112] shown as Fig. 6.1(a), whose input layer and output layer are pulse bursts, and each recurrent hidden layer is a GTI cavity, and the structure of a hidden layer is shown in Fig. 6.1 (b). Forward propagation of a time series through the network is equivalent to sending an input pulse burst through the GTIs, and backpropagation from a single output node yields the impulse response of the cavity set.

(a)   (b)
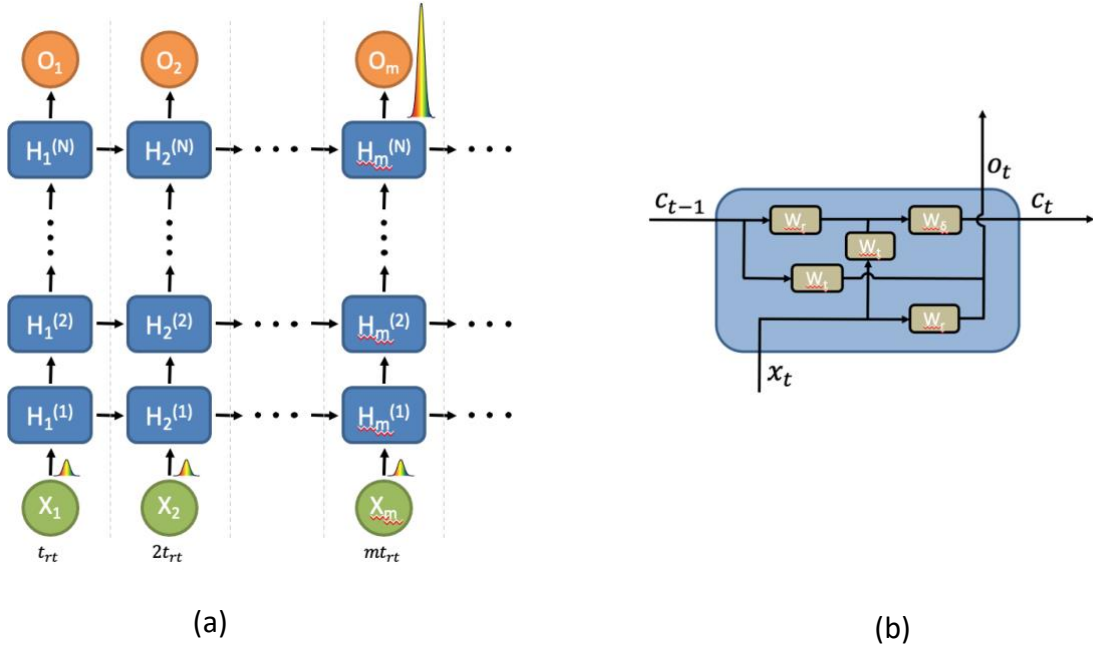
Figure 6. 1: (a) Deep recurrent neural network description of coherent pulse stacking. (b) structure of the hidden layer [112]

$x_t = A_t e^{i\emptyset_{in}}$ is the input layer which corresponds to a time series of modulated pulses. c_t is representative of the stored electric field within the cavity. o_t is a time series of the electric field of the output pulses. Thus, the forward propagation is given by

$$o_t = W_r x_t + W_t c_{t-1}$$

$$c_t = W_\delta (W_r c_{t-1} + W_t x_t) \qquad (6.1)$$

Where $W_r = r$ is the electric field reflectivity of the cavity front mirror; $W_t = it = i(\sqrt{1 - r^2})$, t is the electric field transmission of the cavity front mirror; $W_\delta = \alpha e^{i\delta}$, δ is the cavity phase, and α is the cavity roundtrip loss. Backpropagation of a single stacked output pulse is used to train

76

the neural network until a desirable input pulse burst shape is obtained. The loss function is the mean-square-error between the ideal output pulse intensity and calculated intensity given by:

$$MSE = (I_{ideal} - I_{calc})^2 \qquad (6.2)$$

Thus, the convex optimization algorithm needs to find the optimal values.

6.4 Machine Learning Algorithms for Optimizing Coherent Pulse Stacking

Conventionally, Stochastic Parallel Gradient Descent (SPGD) [110], as a model-free optimizer, can be used in CPS to optimize both the pulse phase and cavity phases to maximize the output power. However, SPGD as a convex optimizer cannot guarantee reaching the global optimal solution given the existence of multiple non-optimal local maxima. Also, as the number of pulses in the stacking sequence increases, convergence speed of the optimization algorithm needs to be improved. In this part, we simulated four cavities and nine input gaussian pulses, which is shown in Fig. 6.2. and use the time reversal method to calculate the cavity phases for these four cavities and optimize 9 pulse phases for improving stacking fidelity using SPGD, momentum stochastic parallel gradient descent (MSPGD) and policy gradient. Among these three methods, we find that MSPGD achieves best performance and can potentially be advantageous for CPS to increase the system operation efficiency [114].
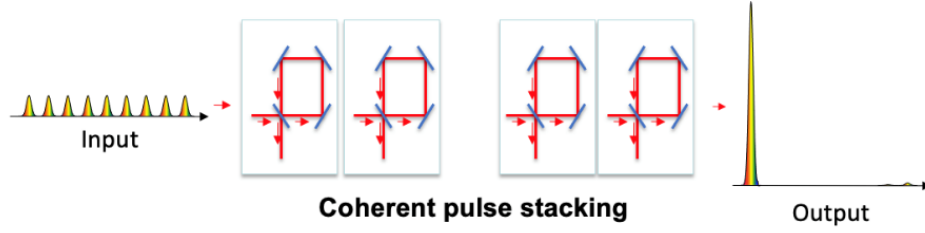
Figure 6. 2: Schematic of a four cavity Coherent Pulse Stacking (CPS) system

The SPGD algorithm is a local convex optimization algorithm that seeks to "climb the hill" toward the local maximum (or minimum). The update rule of the iteration is given by:

$$U^{k+1} = U^k + \gamma \delta J^k \delta U^k \tag{6.3}$$

Where k is the iteration number. $U = \{U_1, U_2, \ldots, U_N\}$ is a controllable vector corresponding to the phase of pulses; N is the number of pulses. γ is the learning rate, which is positive and the hyperparameter in the system; δJ is the output variation of the system performance.

MSPGD is a method that helps SPGD in the relevant direction and dampens oscillations [112]. It does this by adding a fraction η of the update vector of the past time step to the current update vector. The update rule of the iteration is given by:

$$U^{k+1} = U^k + V^k \tag{6.4}$$

$$V^k = (1 - \eta)\gamma \delta J^k \delta U^k + \eta V^{k-1} \tag{6.5}$$

Substituting (6.5) into (6.4):

$$\boldsymbol{U}^{k+1} = \boldsymbol{U}^k + (1-\eta)\gamma\delta J^k \delta\boldsymbol{U}^k + \eta\boldsymbol{V}^{k-1}$$

$$= \boldsymbol{U}^k + (1-\eta)\gamma\delta J^k \delta\boldsymbol{U}^k + \eta(1-\eta)\gamma\delta J^{k-1}\delta\boldsymbol{U}^{k-1} + \eta^2\boldsymbol{V}^{k-2} \qquad (6.6)$$

Obviously, instead of randomly assigning an action in each iteration, it assumes the current update vector has a relationship with previous update vector. The current vector comes from the exponentially weighted average of the historical vector variation rather than only current vector variation. It is easily shown that MSPGD degrades into SPGD if $\eta = 0$, which means the past update variation is independent to the current update vector. Essentially, when adding momentum, we push a ball down a hill. The ball accumulates momentum as it rolls downhill, becoming faster and faster on the way. As shown in Fig. 6.3, the gradient δU gets smaller and smaller when optimizing for SPGD, which is represented by the green solid arrow. However, Momentum SPGD, to some extent, will supplement the gradient, which is represented by the green dashed line. Thus, it can accelerate the convergence speed when training the deep recurrent neural network.
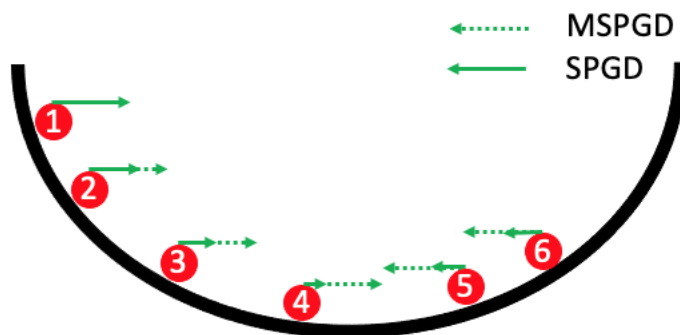
Figure 6. 3: Comparison of SPGD (solid arrow) and MSPGD (dashed arrow), MSPGD accelerate the convergence speed.

In addition, MSPGD can avoid local maximum (or minimum). Since at the local optimal point, even though the gradient δJ^k is zero, the momentum term ηV^{k-1} is non-zero. Compared with SPGD, MSPGD has the momentum to jump out of the local minimum as shown in Fig. 6.4.

(a)   (b)

Figure 6. 4: Comparison of SPGD (a) and MSPGD (b), MSPGD can avoid local minimum point because of the momentum term.

The momentum idea can be effectively shown with a contour plot in Fig. 6.5. Optimizing a cost function with SPGD is like oscillating up and down along the y-axis, and the bigger the oscillation up and down the y-axis, the slower optimizer progress along the x-axis. Intuitively, it then makes sense to add something (e.g., momentum) to help us oscillate less along y-axis, thus moving faster along the x-axis towards the global maximum (minimum). As a result, it leads to faster convergence, reduced oscillation and potentially a better solution.

(a)   (b)
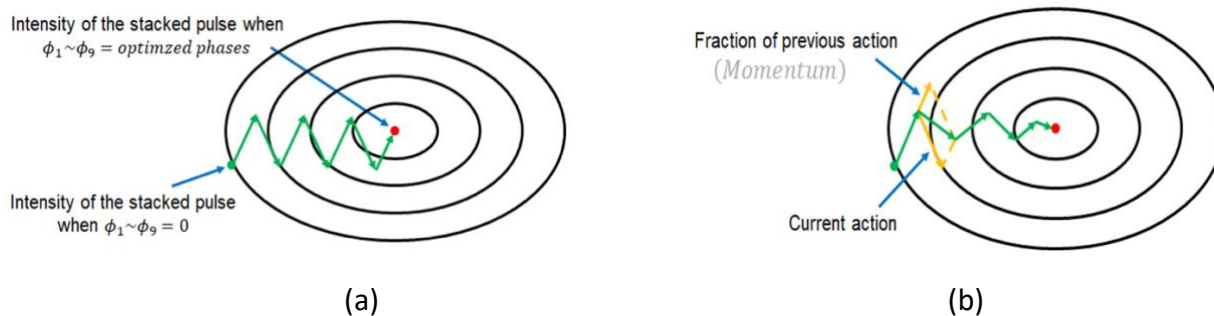
Figure 6. 5: Contour plot of SPGD (a) and MSPG (b)

Policy gradient method [113] as a modal-based reinforcement learning algorithm can be applied to solve the optimal coherent pulse stacking problem. Policy gradient methods assign specific phase variance every step instead of random phase variance like in MSPGD or SPGD. In policy gradient, the initial state S is defined as a random (or zero) vector, which is the phase of each pulse. The reward R is the intensity of the maximum output pulse resulting from the pulse-stacking. The action A is defined as how to tune the phase. Since the action is a combination of continuous real numbers, the action space is too large to be learned for each possible action. For this reason, instead of computing learned probabilities for each action, we found the statistics of the probability distribution of actions by assuming that a policy follows a Gaussian distribution. The probability density function for the action A is defined by:

$$\pi(A|S,\theta) = \frac{1}{(2\pi)^{1/n}|\Sigma|^{1/2}} \exp\left\{-(A-\theta)\Sigma^{-1}(A-\theta)\right\} \tag{6.7}$$

where θ and Σ are the mean and the covariance of the Gaussian distribution. Since our application is simple enough to be modeled as simple relationships, we select θ as a policy parameter and Σ is chosen as a heuristically learned value. We used vanilla reinforce algorithm with gradient ascent to learn the policy parameter θ. An update rule based on the gradient ascent is given by:

$$\theta \leftarrow \theta + \eta \cdot \nabla_\theta J \tag{6.8}$$

where the gradient of the expected return J is estimated by:

$$\nabla_\theta J = (R - B)\nabla_\theta \log \pi(A|S,\theta). \tag{6.9}$$

Where B is the baseline chosen as average of rewards and updated through learning steps in this work. The gradient of a log of a policy π is calculated by:

$$\nabla_\theta \log \pi(A|S, \theta) = \nabla_\theta \left[-\frac{1}{2}(A - \theta)^T \Sigma^{-1}(A - \theta) \right] = \Sigma^{-1}(A - \theta) \qquad (6.10)$$

Let n be the number of input pulses (n=9 in this CPS simulation). The function f(S) calculating a pulse intensity after stacking processes is known. η is a learning rate and N_{iter} is the maximum number of iterations. Flow diagram of vanilla reinforce algorithm is given:

Algorithm	Vanilla REINFORCE

Input: S_0, N_{iter}, η
Initialize: $k \leftarrow 1$, $B_k \leftarrow 0$, $S \leftarrow S_0$
while $k \leq N_{iter}$ **do**
    Randomly assign actions: $A_k \sim N(\theta_k, \Sigma)$
    Compute a reward: $R_k \leftarrow f(S + A_k)$
    Gradient ascent: $\theta_{k+1} \leftarrow \theta_k + \eta \cdot (R_k - B_k)\Sigma^{-1}(A_k - \theta_k)$
    Update a baseline: $B_{k+1} \leftarrow \frac{(B_k \cdot k + R_k)}{k+1}$
    $k \leftarrow k + 1$
end

Fig. 6.6 shows the learning curves of all three algorithms. It is easily seen the output power converged to a value close to 1 for all three algorithms. MSPGD converged fastest with only ~250 episodes. Policy gradient needs ~700 episode to converge. SPGD is the slowest algorithm. Due to the environment noise, we added simulated gaussian random walk noise in the CPS. The policy gradient is sensitive to the noise at the optimal point. Thus, MSPGD has a potential advantage for coherent pulse stacking systems.
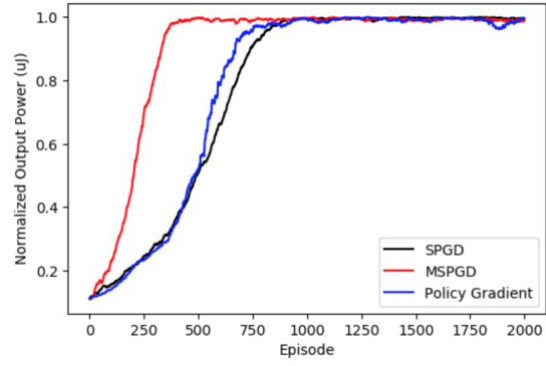
Figure 6. 6: SPGD, MSPGD and Policy Gradient performance in CPS

Chapter 7 Summary and Perspectives

To summarize, this dissertation has accomplished the theoretical study and experimental demonstration of high energy pulse generation in Mid-IR range using Er:ZBLAN fibers, which also suggest the directions to pursue for the future. To be specific, based on the detailed numerical model of this high energy amplification system, we completed a series of 70 µm core Er:ZBLAN LMA fiber high energy amplification experiments with the OPO/OPA seed source operating at low repetition rate of 10 Hz, producing up to 0.7 mJ in ~10 ns pulses at 2.72 µm [65]. The experiments are 3 times improvement over the previous high energy results at these mid-IR wavelengths as shown in Fig.7.1 and also demonstrated potential of Er:ZBLAN LMA fibers for achieving mJ-range output pulse energies. Furthermore, we first demonstrated single transverse mode high energy, high rep-rate, nanosecond short pulses in the mid-IR wavelength range using large core Er:ZBLAN fiber amplifiers [116]. The single mode highest record energies (Fig. 7.1) achieved are ~750 µJ at 2.78-µm in ~100ns, 1kHz pulses, obtained with a 50-µm diameter core fiber amplifier pumped at 976 nm [115]. These nanosecond pulses amplification results enable us to pursue ultrashort pulses high energy amplifications. The chirped pulse amplification (CPA) system including Offner stretcher, compressor and multiple amplifier stages are designed to amplify the ultrashort pulses. In the future, we will experimentally build the Mid-IR fiber CPA, which has potential to generate ~mJ level

femtosecond lasers at 2.7µm due to the broad spectral bandwidth signal from nonlinear amplifiers. Since of the nonlinear and optical damage limitation of CPAs, we purse to use the time and spectral domain coherent combining techniques in Mid-IR spectral range to achieve ~10mJ femtosecond pulses. In terms of that, we proposed several novel machine learning algorithms for optimizing coherent beam combination. The simulation results show the effectiveness and superiorities in 1µm CCC fiber based CPSA system [114]. We plan to experimentally transfer these techniques into 2.8µm range in the near future. The other published achievements during my PhD have been listed in bibliography [116,117].
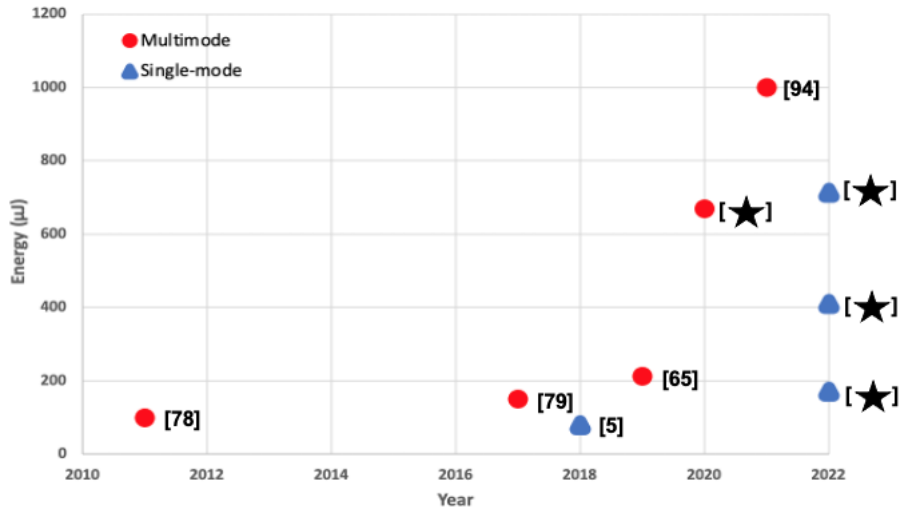
Figure 7. 1: Summarization of high energy results at ~2.8µm using fluoride fibers. The ★ represents results in this thesis.

Bibliography

1. A. Einstein, "On the quantum theory of radiation," in Laser Theory, F. A. Barnes, ed., pp. 5–21, IEEE Press, New York (1972).

2. Townes, C. H. (1951). Atomic clocks and frequency stabilization on microwave spectral lines. Journal of Applied Physics, 22(11), 1365-1372.

3. Gordon, James P., Herbert J. Zeiger, and Charles H. Townes. "Molecular microwave oscillator and new hyperfine structure in the microwave spectrum of N H 3." Physical Review 95.1 (1954): 282.

4. Maiman, Theodore H. "Stimulated optical radiation in ruby." (1960): 493-494.

5. https://optics.org/news/3/10/44

6. Minelly, J. D., Taylor, E. R., Jedrzejewski, K. P., Wang, J. & Payne, D. N. Laser-diode-pumped Nd-doped fibre laser with output power>lW. Paper 246 in Proc. CLEO (1992).

7. Dominic, V. et al. 110 W fibre laser. Electron. Lett. 35, 1158–1160 (1999).

8. Sacks, Zachary S., Zeev Schiffer, and Doron David. "Long wavelength operation of double-clad Tm: silica fiber lasers." Fiber Lasers IV: Technology, Systems, and Applications. Vol. 6453. International Society for Optics and Photonics, 2007.

9. Amini-Nik, Saeid, et al. "Ultrafast mid-IR laser scalpel: protein signals of the fundamental limits to minimally invasive surgery." PLoS one 5.9 (2010): e13053.

10. Aydin, Yiğit Ozan. "Development of high-power 3 μm fiber laser sources and components." (2019).

11. C. Bader and I. Krejci, "Indications and limitations of Er:YAG laser applications in dentistry," American Journal of Dentistry, vol. 19, no. 3, pp. 178–186, 2006.

12. C. K. Chen, N. J. Chang, J. H. Ke, E. Fu, and W. H. Lan, "Er:YAG laser application for removal of keratosis using topical anesthesia," Journal of Dental Sciences, vol. 8, no. 2, pp. 196–199, 2013.

13. G. Teikemier and D. J. Goldberg, "Skin resurfacing with the erbium:YAG laser," Dermatologic Surgery, vol. 23, no. 8, pp. 685–687, 1997.

14. R. F. Bonner, L. G. Prevosti, M. B. Leon, K. Levin, and D. Tran, "New source for laser angioplasty: Er:YAG laser pulses transmitted through zirconium fluoride optical fiber catheters," in SPIE Proc., vol. 0906, 1988, pp. 288–293.

15. J. M. Teichman, K. F. Chan, P. P. Cecconi, N. S. Corbin, A. D. Kamerer, R. D. Glickman, and A. J. Welch, "Erbium:YAG versus holmium:YAG lithotripsy," Journal of Urology, vol. 165, no. 3, pp. 876–879, 2001.

16. Z. Li, L. Reinisch, and W. P. Van de Merwe, "Bone ablation with Er:YAG and CO2 laser: Study of thermal and acoustic effects," Lasers in Surgery and Medicine, vol. 12, no. 1, pp. 79–85, 1992.

17. C. C. Neubaur and G. Stevens, "Erbium:YAG laser cataract removal: Role of fiber-optic delivery system," Journal of Cataract & Refractive Surgery, vol. 25, no. 4, pp. 514–520, 1999.

18. D. G. Panduric, I. Bago, D. Katanec, J. Žabkar, I. Miletić, and I. Anić, "Comparison of Er:YAG laser and surgical drill for osteotomy in oral surgery: an experimental study," Journal of Oral and Maxillofacial Surgery, vol. 70, no. 11, pp. 2515–2521, 2012.

19. M. H. Niemz, "Interaction Mechanism," in Laser-Tissue Interactions, E. Greenbaum and O. Ridge, Eds. Springer Berlin Heidelberg, 2007, pp. 45–150.

20. Pierce, Mark C., et al. "Laser-tissue interaction with a continuous wave 3-μm fibre laser: Preliminary studies with soft tissue." Lasers in Surgery and Medicine: The Official Journal of the American Society for Laser Medicine and Surgery 26.5 (2000): 491-495.

21. Schliesser, Albert, Nathalie Picqué, and Theodor W. Hänsch. "Mid-infrared frequency combs." Nature photonics 6.7 (2012): 440-449.

22. Yang, Weiqiang, et al. "High power all fiber mid-IR supercontinuum generation in a ZBLAN fiber pumped by a 2 μm MOPA system." Optics Express 21.17 (2013): 19732-19742

23. Majewski, Matthew R., Robert I. Woodward, and Stuart D. Jackson. "Dysprosium-doped ZBLAN fiber laser tunable from 2.8 μm to 3.4 μm, pumped at 1.7 μm." Optics letters 43.5 (2018): 971-974.

24. Woodward, R. I., et al. "Swept-wavelength mid-infrared fiber laser for real-time ammonia gas sensing." APL photonics 4.2 (2019): 020801.

25. Huang, H., et al. "Ultra-broadband long-wave-infrared pulse production using a chirped-pulse difference-frequency generation." *Optics Letters* 47.13 (2022): 3159-3162.

26. Mahulikar, Shripad P., Hemant R. Sonawane, and G. Arvind Rao. "Infrared signature studies of aerospace vehicles." Progress in aerospace sciences 43.7-8 (2007): 218-245.

27. X. Xiao, H. Huang, W. Du, J. Nees, A. Galvanauskas, and I. Jovanovic, "Progress in development of an ultrafast power-scalable long-wave infrared parametric source," Ultrafast Optics XII, Bol, Croatia, October 6-11, 2019.

28. Keldysh, L. V. "Ionization in the field of a strong electromagnetic wave." Sov. Phys. JETP 20.5 (1965): 1307-1314.

29. Wolter, Benjamin, et al. "Strong-field physics with mid-IR fields." Physical Review X 5.2 (2015): 021034.

30. Colosimo, P., et al. "Scaling strong-field interactions towards the classical limit." Nature Physics 4.5 (2008): 386-389.

31. Popmintchev, Tenio, et al. "Bright coherent ultrahigh harmonics in the keV x-ray regime from mid-infrared femtosecond lasers." science 336.6086 (2012): 1287-1291.

32. Jovanovic, Igor, Guibao Xu, and Scott Wandel. "Mid-infrared laser system development for dielectric laser accelerators." Physics Procedia 52 (2014): 68-74.

33. Woodbury, D., Feder, L., Shumakova, V., Gollner, C., Schwartz, R., Miao, B., ... & Milchberg, H. M. (2018). Laser wakefield acceleration with mid-IR laser pulses. Optics letters, 43(5), 1131-1134.

34. Jeong, Y. el, et al. "Ytterbium-doped large-core fiber laser with 1.36 kW continuous-wave output power." Optics express12.25 (2004): 6088-6092.

35. Wu, Jianfeng, et al. "Highly efficient high-power thulium-doped germanate glass fiber laser." Optics letters 32.6 (2007): 638-640.

36. Spiegelberg, Christine, et al. "Low-noise narrow-linewidth fiber laser at 1550 nm (June 2003)." Journal of Lightwave Technology 22.1 (2004): 57-62.

37. M. Poulain, M. Poulain, J. Lucas, and P. Brun, "Verres fluorés au tétrafluorure de zirconium: propriétés optiques d'un verre dopé au Nd^{3+}," Materials Research Bulletin, vol. 10, no. 4, pp. 243–246, 1975.

38. Shibata, Shuichi, et al. "Prediction of loss minima in infra-red optical fibres." Electronics Letters 21.17 (1981): 775-777.

39. Cozic, S., S. Poulain, and M. Poulain. "Low loss fluoride optical fibers: Fabrication and applications." Specialty Optical Fibers. Optica Publishing Group, 2018.

40. Cozmuta, Ioana, et al. "Breaking the silica ceiling: ZBLAN-based opportunities for photonics applications." Optical Components and Materials XVII. Vol. 11276. SPIE, 2020.

41. Saad, Mohammed. "Indium fluoride glass fibers." Laser Refrigeration of Solids V. Vol. 8275. SPIE, 2012.

42. Gauthier, Jean-Christophe, et al. "Mid-IR supercontinuum from 2.4 to 5.4 μm in a low-loss fluoroindate fiber." Optics Letters 41.8 (2016): 1756-1759.

43. Colaizzi, James, and M. John Matthewson. "Mechanical durability of ZBLAN and aluminum fluoride-based optical fiber." Journal of lightwave technology 12.8 (1994): 1317-1324.

44. Aydın, Y. O., Fortin, V., Maes, F., Jobin, F., Jackson, S. D., Vallée, R., & Bernier, M. (2017). Diode-pumped mid-infrared fiber laser with 50% slope efficiency. Optica, 4(2), 235-238.

45. Newburgh, G. A., and M. Dubinskii. "Power and efficiency scaling of Er: ZBLAN fiber laser." Laser Physics Letters 18.9 (2021): 095102.

46. Zhu, Xiushan, and N. Peyghambarian. "High-power ZBLAN glass fiber lasers: review and prospect." Advances in OptoElectronics 2010 (2010).

47. Aydin, Yigit Ozan, et al. "Towards Power Scaling of 2.8 μm Fiber Lasers." Optics letters 43.18 (2018): 4542-4545.

48. Du, W., Xiao, X., Cui, Y., Chen, M., Jovanovic, I., & Galvanauskas, A. (2019, May). High Energy Er: ZBLAN LMA Fiber Amplifier Producing~ 200μJ and~ 10ns Pulses at 2.72 μm. In CLEO: Science and Innovations (pp. SF2L-5). Optica Publishing Group.

49. Jeff Koplow, et al. "Fused-silica damage threshold established at 1064 nm" Laser Focus World (2018)

50. Aydin, Yigit Ozan, et al. "Endcapping of high-power 3 μm fiber lasers." Optics Express 27.15 (2019): 20659-20669.

51. Lecoq, André, and Marcel Poulain. "Fluoride glasses in the ZrF4,BaF2, YF3,AlF3 quaternary system." Journal of Non-Crystalline Solids 41.2 (1980): 209-217

52. Zhang, Lipeng, Fuxi Gan, and Paul Wang. "Evaluation of refractive-index and material dispersion in fluoride glasses." Applied optics 33.1 (1994): 50-56.

53. Dutton, Harry JR. Understanding optical communications. Vol. 1. New Jersey: Prentice Hall PTR, 1998.

54. Jackson, Stuart D., Terence A. King, and Markus Pollnau. "Diode-pumped 1.7-W erbium 3-µm fiber laser." Optics letters 24.16 (1999): 1133-1135.

55. Jackson, S. D., T. A. King, and Markus Pollnau. "Efficient high power operation of erbium 3 µm fibre laser diode-pumped at 975 nm." Electronics letters 36.3 (2000): 223-224.

56. Zhu, Xiushan, and Ravi Jain. "Numerical analysis and experimental results of high-power Er/Pr: ZBLAN 2.7 µm fiber lasers with different pumping designs." Applied Optics 45.27 (2006): 7118-7125.

57. Wetenkamp, L., G. F. West, and H. Többen. "Co-doping effects in erbium3+-and holmium3+-doped ZBLAN glasses." Journal of non-crystalline solids 140 (1992): 25-30.

58. Jackson, Stuart D., Markus Pollnau, and Jianfeng Li. "Diode pumped erbium cascade fiber lasers." IEEE journal of quantum electronics 47.4 (2011): 471-478.

59. Jackson, S. D. "High-power erbium cascade fibre laser." Electronics letters 45.16 (2009): 1.

60. Schneider, Jutta. "Mid-infrared fluoride fiber lasers in multiple cascade operation." IEEE photonics technology letters 7.4 (1995): 354-356.

61. Pollnau, Markus, et al. "Three-transition cascade erbium laser at 1.7, 2.7, and 1.6 µm." Optics letters 22.9 (1997): 612-614.

62. Du, W., Xiao, X., Cui, Y., Nees, J., Jovanovic, I., & Galvanauskas, A. (2019, September). 0.7 mJ and 12ns Pulses at 2.72 µm from a 70µm Core Er: ZBLAN Fiber Amplifier. In Advanced Solid State Lasers (pp. AM4A-6). Optical Society of America.

63. Cui, Y., Du, W., Chen, M., & Galvanauskas, A. (2021, May). Generation of 95 fs mid-IR pulses with 1.8 W average power using an Er: ZrF 4 fiber mode-locked oscillator and a nonlinear amplifier. In 2021 Conference on Lasers and Electro-Optics (CLEO) (pp. 1-2). IEEE.

64. Cui, Y., Chen, M., Du, W., Bai, Y., & Galvanauskas, A. (2021). Generation of 85 fs mid-IR pulses with up to 2.4 W average power using an Er: ZBLAN fiber mode-locked oscillator and a nonlinear amplifier. Optics Express, 29(26), 42924-42931.

65. Du, W., Xiao, X., Cui, Y., Nees, J., Jovanovic, I., & Galvanauskas, A. (2020). Demonstration of 0.67-mJ and 10-ns high-energy pulses at 2.72 µm from large core Er: ZBLAN fiber amplifiers. Optics Letters, 45(19), 5538-5541.

66. Knowles, David S., and Hans P. Jenssen. "Upconversion versus Pr-deactivation for efficient 3 mu m laser operation in Er." IEEE journal of quantum electronics 28.4 (1992): 1197-1208.

67. Li, Jianfeng, and Stuart D. Jackson. "Numerical modeling and optimization of diode pumped heavily-erbium-doped fluoride fiber lasers." IEEE Journal of Quantum Electronics 48.4 (2012): 454-464.

68. Gorjan, Martin, Marko Marinček, and Martin Čopič. "Role of interionic processes in the efficiency and operation of erbium-doped fluoride fiber lasers." IEEE Journal of Quantum Electronics 47.2 (2011): 262-273.

69. Henderson-Sapir, Ori. Development of dual-wavelength pumped mid-infrared fibre laser. Diss. 2015.

70. Jackson, Stuart, et al. "Spectroscopy of the rare-earth-ion transitions in fluoride glasses." Mid-Infrared Fiber Photonics. Woodhead Publishing, 2022. 333-399.

71. Chen, Siyun. Spectral and Temporal Control of Broadband Pulses to Enable Multi-TW Peak Power Coherently-Combined Fiber Laser Arrays. Diss. 2021.

72. Butcher, John C. "On the implementation of implicit Runge-Kutta methods." BIT Numerical Mathematics 16.3 (1976): 237-240.

73. Sauer, Timothy. "Numerical solution of stochastic differential equations in finance." Handbook of computational finance. Springer, Berlin, Heidelberg, 2012. 529-550.

74. P. S. Golding, S. D. Jackson, T. A. King, and M. Pollnau, "Energy transfer processes in Er3+-doped and Er3+, Pr3+-codoped ZBLAN glasses," Phys. Rev. B 62, 856–864 (2000).

75. Zhu, Xiushan, and Ravi Jain. "Compact 2 W wavelength-tunable Er: ZBLAN mid-infrared fiber laser." Optics letters 32.16 (2007): 2381-2383.

76. Sandrock, T., et al. "High-power continuous-wave upconversion fiber laser at room temperature." Optics letters 22.11 (1997): 808-810.

77. Tokita, Shigeki, et al. "Liquid-cooled 24 W mid-infrared Er: ZBLAN fiber laser." Optics letters 34.20 (2009): 3062-3064.

78. Tokita, Shigeki, et al. "12 WQ-switched Er: ZBLAN fiber laser at 2.8 μm." Optics letters 36.15 (2011): 2812-2814.

79. Shen, Yanlong, et al. "High Peak Power Actively Q-switched Mid-infrared Fiber Lasers at 3 μm." Applied Physics B 123.4 (2017): 105.

80. Jackson, Stuart D. "Towards high-power mid-infrared emission from a fibre laser." Nature photonics 6.7 (2012): 423.

81. Zhou, P., et al. "Review on recent progress on mid-infrared fiber lasers." Laser Physics 22.11 (2012): 1744-1751.

82. Frerichs, Ch, and T. Tauermann. "Q-switched operation of laser diode pumped erbium-doped fluorozirconate fibre laser operating at 2.7 mu m." Electronics Letters 30.9 (1994): 706-707.

83. Libatique, N. J. C., et al. "A compact diode-pumped passively Q-switched mid-IR fiber laser." Advanced Solid State Lasers. Optical Society of America, 2000.

84. Frerichs, Christian, and Udo B. Unrau. "Passive Q-switching and mode-locking of erbium-doped fluoride fiber lasers at 2.7 μm." Optical Fiber Technology 2.4 (1996): 358-366.

85. Tokita, Shigeki, et al. "12 WQ-switched Er: ZBLAN fiber laser at 2.8 μm." Optics letters 36.15 (2011): 2812-2814.

86. Shen, Yanlong, et al. "High Peak Power Actively Q-switched Mid-infrared Fiber Lasers at 3 μm." Applied Physics B 123.4 (2017): 105.

87. Xiao, X., J. A. Nees, and I. Jovanovic. "High-energy nanosecond parametric source at 2.7 μm." Applied Optics 60.13 (2021): 3585-3590.

88. Xiao, Xuan. Broadband Long-wave Infrared Few-cycle Pulse Generation via Optical Parametric Chirped-pulse Amplification. Diss. 2021.

89. Frantz, Lee M., and John S. Nodvik. "Theory of pulse propagation in a laser amplifier." Journal of Applied Physics 34.8 (1963): 2346-2349.

90. Siegman, A. E. "Design considerations for laser pulse amplifiers." Journal of Applied Physics 35.2 (1964): 460-460.

91. Agrawal, Govind P. "Nonlinear fiber optics: its history and recent progress." JOSA B 28.12 (2011): A1-A10.

92. Chichkov, Nikolai B., et al. "Amplification of nanosecond pulses in a single-mode erbium-doped fluoride fibre amplifier." IEEE Photonics Technology Letters (2022).

93. Agger, Christian, et al. "Supercontinuum generation in ZBLAN fibers—detailed comparison between measurement and simulation." JOSA B 29.4 (2012): 635-645.

94. Aydin, Yiğit Ozan, et al. "Dual stage fiber amplifier operating near 3 μm with milijoule-level, sub-ns pulses at 5 W." Optics Letters 46.18 (2021): 4506-4509.

95. Sójka, Lukasz, et al. "High Peak Power Q-switched Er: ZBLAN Fiber Laser." Journal of Lightwave Technology 39.20 (2021): 6572-6578

96. Shen, Yanlong, et al. "200 µJ, 13 ns Er: ZBLAN mid-infrared fiber laser actively Q-switched by an electro-optic modulator." Optics Letters 46.5 (2021): 1141-1144.

97. Fermann, Martin E. "Single-mode excitation of multimode fibers with ultrashort pulses." Optics Letters 23.1 (1998): 52-54.

98. Stutzki, Fabian, et al. "Designing advanced very-large-mode-area fibers for power scaling of fiber-laser systems." Optica 1.4 (2014): 233-242.

99. Marcuse, D. "Theory of Optical Dielectric Waveguides." Acad. Press, NY (1974).

100. Snyder, A. W., and J. D. Love. "Optical waveguide theory chapman and hall." New York 66 (1983).

101. Gloge, Detlef. "Weakly guiding fibers." Applied optics 10.10 (1971): 2252-2258.

102. Galvanauskas, Almantas, et al. "High peak power pulse amplification in large-core Yb-doped fiber amplifiers." IEEE Journal of selected topics in quantum electronics 13.3 (2007): 559-566.

103. Koplow, Jeffrey P., Dahv AV Kliner, and Lew Goldberg. "Single-mode operation of a coiled multimode fiber amplifier." Optics letters 25.7 (2000): 442-444.

104. A. W. Snyder, and J. D. Love, "Reflection at a curved dielectric interface – electromagnetic tunneling," IEEE Trans. on Microwave Theory and Techniques Vol. MTT-23, No. 1, 134– 141, 1975.

105. Schermer, Ross T., and James H. Cole. IEEE Journal of Quantum Electronics 43.10 (2007): 899-909.

106. Li, L., Li, C., Chen, X., Liu, L., & Wu, J. (2014, November). Analysis of chirped-pulse-amplification system based on Offner triplet stretcher and transmission grating compressor. In High-Power Lasers and Applications VII (Vol. 9266, pp. 325-331). SPIE.

107. Hartmann, P., Jedamzik, R., Carré, A., Krieg, J., & Westerhoff, T. (2021). Glass ceramic ZERODUR®: Even closer to zero thermal expansion: a review, part 1. Journal of Astronomical Telescopes, Instruments, and Systems, 7(2), 020901.

108. Gao, Y., Li, J. F., Wang, Y. Z., Shi, Y. W., Liu, F., Li, K., ... & Liu, Y. (2018). Design of ultra large normal dispersion ZBLAN photonic crystal fiber and its application in Mid-IR ultra short fiber lasers. IEEE Photonics Journal, 10(6), 1-9.

109.   T. Zhou, J. Ruppe, C. Zhu, I. Hu, J. Nees, and A. Galvanauskas, "Coherent pulse stacking amplification using low-finesse Gires-Tournois interferometers," Opt. Express 23, 7442-7462 (2015).

110.   Ruppe, John. Theoretical and experimental foundations of coherent pulse stacking amplification. Diss. 2017.

111.   Pei, H., Whittlesey, M., Du, Q., & Galvanauskas, A. (2021, May). Design and Operation of Coherent Pulse Stacking Amplification as a Deep Recurrent Neural Network. In CLEO: Science and Innovations (pp. STu2E-2). Optica Publishing Group.

112.   Yang, Guoqing, et al. "Incoherent beam combining based on the momentum SPGD algorithm." Optics & Laser Technology 101 (2018): 372-378.

113.   Sutton, Richard S., and Andrew G. Barto. Reinforcement learning: An introduction. MIT press, 2018.

114.   Du, W., Hyeon, E., Pei, H., Huang, Z., Cheong, Y., Zheng, S., & Galvanauskas, A. (2021, May). Improved Machine Learning Algorithms for Optimizing Coherent Pulse Stacking Amplification. In CLEO: QELS_Fundamental Science (pp. JTh3A-1). Optical Society of America.

115.   Du, W., Chen, M., Cui, Y., Bai, Y., & Galvanauskas, A. (2022, May). Single Mode High Energy Amplification in Mid-IR Using Large Core Er: ZBLAN Fiber Amplifiers. In CLEO: Science and Innovations (pp. SM5L-4). Optica Publishing Group.

116.   Du, Weizhi, Qichen Fu, and Zhengyu Huang. "A Self-Supervised Deep Model for Focal Stacking." CLEO: QELS_Fundamental Science. Optica Publishing Group, 2022.

117.   Huang, Zhengyu, Weizhi Du, and Theodore B. Norris. "Unsupervised Learning Based Focal Stack Camera Depth Estimation." arXiv preprint arXiv:2203.07904 (2022).